Asymmetrical tidal tails of open star clusters: stars crossing their cluster's prah challenge Newtonian gravitation

Pavel Kroupa, Tereza Jerabkova, Ingo Thies, Jan Pflamm-Altenburg, Benoit Famaey, Henri M.J. Boffin, Jörg Dabringhausen, Giacomo Beccari, Timo Prusti, Christian Boily, et al.

Monthly Notices of the ROYAL ASTRONOMICAL SOCIETY
MNRAS **517,** 3613–3639 (2022) https://doi.org/10.1093/mnras/stac2563

Asymmetrical tidal tails of open star clusters: stars crossing their cluster's práh† challenge Newtonian gravitation

Pavel Kroupa [1,2]★ Tereza Jerabkova [3]★ Ingo Thies,[2] Jan Pflamm-Altenburg,[2] Benoit Famaey [4] Henri M. J. Boffin [3] Jörg Dabringhausen [1] Giacomo Beccari [3] Timo Prusti,[5] Christian Boily,[5] Hosein Haghi,[6] Xufen Wu [7,8] Jaroslav Haas,[1] Akram Hasani Zonoozi,[2,6] Guillaume Thomas,[9,10] Ladislav Šubr[1] and Sverre J. Aarseth[11]

[1]*Faculty of Mathematics and Physics, Astronomical Institute, Charles University in Prague, V Holešovičkách 2, CZ-180 00 Praha 8, Czech Republic*
[2]*Helmholtz-Institut für Strahlen- und Kernphysik, University of Bonn, Nussallee 14-16, D-53115 Bonn, Germany*
[3]*European Southern Observatory, Karl-Schwarzschild-Strasse 2, D-85748 Garching bei München, Germany*
[4]*Observatoire Astronomique de Strasbourg, 11, rue de l'Université, F-67000 Strasbourg, France*
[5]*European Space Research and Technology Centre (ESA ESTEC), Keplerlaan 1, NL-2201 AZ Nordwijk, Netherlands*
[6]*Department of Physics, Institute for Advanced Studies in Basic Sciences (IASBS), PO Box 11365-9161, Zanjan, Iran*
[7]*CAS Key Laboratory for Research in Galaxies and Cosmology, Department of Astronomy, University of Science and Technology of China, Hefei, 230026, P. R. China*
[8]*School of Astronomy and Space Science, University of Science and Technology of China, Hefei 230026, China*
[9]*Instituto de Astrofísica de Canarias, E-38205 La Laguna, Tenerife, Spain*
[10]*Universidad de La Laguna, Dpto. Astrofísica, E-38206 La Laguna, Tenerife, Spain*
[11]*Institute of Astronomy, University of Cambridge, Madingley Road, Cambridge CB3 0HA, UK*

Accepted 2022 September 4. Received 2022 September 2; in original form 2021 December 5

ABSTRACT

After their birth a significant fraction of all stars pass through the tidal threshold (práh) of their cluster of origin into the classical tidal tails. The asymmetry between the number of stars in the leading and trailing tails tests gravitational theory. All five open clusters with tail data (Hyades, Praesepe, Coma Berenices, COIN-*Gaia* 13, NGC 752) have visibly more stars within $d_{\rm cl} \approx 50$ pc of their centre in their leading than their trailing tail. Using the Jerabkova-compact-convergent-point (CCP) method, the extended tails have been mapped out for four nearby 600–2000 Myr old open clusters to $d_{\rm cl} > 50$ pc. These are on near-circular Galactocentric orbits, a formula for estimating the orbital eccentricity of an open cluster being derived. Applying the Phantom of Ramses code to this problem in Newtonian gravitation the tails are near-symmetrical. In Milgromian dynamics (MOND), the asymmetry reaches the observed values for $50 < d_{\rm cl}/{\rm pc} < 200$ being maximal near peri-galacticon, and can slightly invert near apo-galacticon, and the Küpper epicyclic overdensities are asymmetrically spaced. Clusters on circular orbits develop orbital eccentricity due to the asymmetrical spill-out, therewith spinning up opposite to their orbital angular momentum. This positive dynamical feedback suggests Milgromian open clusters to demise rapidly as their orbital eccentricity keeps increasing. Future work is necessary to better delineate the tidal tails around open clusters of different ages and to develop a Milgromian direct n-body code.

Key words: gravitation – methods: numerical – Galaxy: kinematics and dynamics – Galaxy: stellar content – open clusters and associations: individual: Hyades, Praesepe, Coma Berenices, COIN-*Gaia* 13, NGC 752, NGC 2419, Pal 5, Pal 14, GD-1 – solar neighbourhood.

1 INTRODUCTION

A galaxy is not populated by stars randomly, because observations show stars to form predominantly as binary systems in embedded clusters which emanate from sub-pc density maxima of molecular clouds (Kroupa 1995a,b; Lada & Lada 2003; Porras et al. 2003; Marks & Kroupa 2011; Megeath et al. 2016; Dinnbier, Kroupa & Anderson 2022a). The properties of these change with galactocentric distance as a result of the varying local gas density (Pflamm-Altenburg & Kroupa 2008; Pflamm-Altenburg, González-Lópezlira & Kroupa 2013; Miville-Deschênes, Murray & Lee 2017; Djordjevic et al. 2019; Wirth et al. 2022). Depending on the number of embedded clusters and their masses, a molecular cloud can spawn an OB association upon the expulsion of residual gas (e.g. Dinnbier & Walch 2020; Dabringhausen, Marks & Kroupa 2022). The kinematical state of the molecular cloud (e.g. it may be contracting if it formed from converging gas flows) defines if the OB association is expanding, still or contracting, or it may even be a mixture of these states (e.g. Wright et al. 2019; Kuhn et al. 2020; Armstrong et al. 2022 for evidence for complicated kinematics).

★ E-mail: pkroupa@uni-bonn.de (PK); Tereza.Jerabkova@eso.org (TJ)
† See Acknowledgements for an explanation of 'práh'.

Thus, the expansion due to gas-expulsion of a very young cluster can be masked by the still-ongoing radial infall of very young stars from the surrounding molecular cloud. Overall, the embedded clusters expand due to expulsion of their residual gas to the sizes of the observed open clusters (Banerjee & Kroupa 2017).

Each young open cluster is therefore expected to be surrounded by a *natal cocoon* of stars. This natal cocoon consists (i) of coeval stars lost through the gas expulsion process forming a tidal tail I (Kroupa, Aarseth & Hurley 2001; Moeckel & Bate 2010; Dinnbier & Kroupa 2020a,b), and (ii) of stars that are nearly co-eval and which formed in other embedded clusters within the same molecular cloud (Dinnbier & Kroupa 2020a,b). The shape and extend of (i) and (ii) can be used to age-date the cluster (Dinnbier et al. 2022b). Evidence for natal cocoons around young (30−300 Myr aged) open clusters have been found and named 'coronae' (Meingast, Alves & Rottensteiner 2021) or 'haloes' (Bouma et al. 2021). Extreme examples of such natal cocoons are the recently discovered few-dozen-Myr old relic filaments that are interlaced with very young open clusters (Jerabkova et al. 2019; Beccari, Boffin & Jerabkova 2020). As the open cluster ages, the natal cocoon expands and thins out while the classical kinematically cold tidal tail (referred to as 'tidal tail II') develops over time through energy-equipartition driven evaporation (Henon 1969; Baumgardt, Hut & Heggie 2002; Heggie & Hut 2003). For velocities $\approx$1 km s^{-1} of the outgoing stars and at an age >200 Myr, the natal cocoon has largely dispersed from the $\approx$200 pc region around the cluster, and the evaporating open cluster has grown a detectable classical cold kinematical tidal tail II (Dinnbier & Kroupa 2020a,b).

The above processes contribute together with resonances and perturbations to a complex distribution of Galactic disc stars in phase space. The purpose of this contribution is to consider the particular process of how stars spill from their open cluster into the Galactic field in view of the newly-discovered asymmetry of the tidal tail[1] around the Hyades open cluster by Jerabkova et al. (2021). The asymmetry is a potentially decisive diagnostic as to the nature of gravitation, which drives cluster dissolution through the process of energy equipartition within the cluster. As demonstrated in an accompanying publication (Pflamm-Altenburg et al., in preparation) in Newtonian gravitation and for a smooth Galactic potential, the leading and tidal tail must be symmetric within Poisson noise due to the finite number of stars. The ESO/ESA team (Boffin et al. 2022; Jerabkova et al., in preparation) has now used the *Gaia* eDR3 to map out the extended tidal tails of three further open clusters (Praesepe, Coma Berenices, NGC 752) with ages in the range 600–2000 Myr. As calculated by Pflamm-Altenburg et al. (in preparation), the null hypothesis that the tails of Hyades and NGC 752 show the Newtonian symmetry is in tension with the data with more than 6.5 and 1.3 sigma confidence, respectively (the leading tail having more stars in both cases). An asymmetry can arise through a very specific perturbation (Jerabkova et al. 2021), but the same perturbation cannot have affected the Hyades and NGC 752 in a similar manner. Here the alternative hypothesis is tested if Milgromian gravitation, which is non-linear and thus leads to a lopsided equipotential surface around an open cluster (Wu, Zhao & Famaey 2010; Wu et al. 2017) can account for the amplitude and sign of the observed asymmetries. This contribution constitutes a first explorative step towards relaxational stellar dynamics in Milgromian gravitation such that this topic can only be superficially skimmed pointing out, where a future significant research effort is needed to deepen our understanding of the observed phenomena on star-cluster scales.

[1]Unless otherwise stated, 'tidal tail' will refer to the classical tidal tail II.

In the following, the formation and properties of tidal tails and the observed extended tidal tails of four open clusters are described (Section 2). Milgromian gravitation is introduced in Section 3 with the here-applied simulation method of tidal tails. The models are documented in Section 4. Section 5 contains the results with Section 5.5 outlining the formation and evolution of embedded clusters through the Newtonian into the Milgromian regime. The conclusions with a discussion and an outline for future work are provided in Section 6.

2 OPEN CLUSTERS AND THEIR TIDAL TAILS

The tidal tail of a star cluster contains fundamental information on the nature of gravitation, and a brief discussion of its formation and evolution around an initially virialized star cluster in Newtonian gravitation is provided (Section 2.1). This is followed by a discussion of the extraction and properties of real tidal tails (Section 2.2).

2.1 The decomposition of open star clusters into their galaxy

Baumgardt & Makino (2003) performed direct Newtonian n-body models of initially virialized clusters of different initial masses $M_{\rm oc,0}$. These orbit in a spherical logarithmic Galactic potential. During the first $\approx$50 Myr, a cluster looses about 30 per cent of its initial mass due to stellar evolution, assuming it to be populated with a canonical stellar initial mass function (IMF, Kroupa 2001). After these $\approx$50 Myr, an open cluster evolves through two-body-relaxation-driven evaporation that continuously pushes stars across its tidal práh, thereby populating the classical tidal tail II. The cluster thus slowly dissolves with a near-constant mass-loss rate, $\dot{M}_{\rm oc} \approx 0.7\, M_{\rm oc,0}/T_{\rm diss,0}$. The lifetime of an open cluster starting with a canonical IMF (average stellar mass $\bar{m} \approx 0.55{\rm M}_\odot$, table 4-1 in Kroupa et al. 2013) can be approximated to be (equation7 in Baumgardt & Makino 2003)

$$\frac{T_{\rm diss}}{\rm Myr} \approx 0.86\, G^{-\frac{1}{2}} \left[\frac{M_{\rm oc}}{\bar{m}\ln(0.02\, M_{\rm oc}/\bar{m})}\right]^{0.79}, \quad (1)$$

where $G \approx 0.0045\,{\rm M}_\odot^{-1}\,{\rm pc}^3\,{\rm Myr}^{-2}$ is the gravitational constant. Thus, a very young open cluster weighing $M_{\rm oc,0} = 1300{\rm M}_\odot (= M_{\rm oc})$ dissolves within $T_{\rm diss,0} \approx 2$ Gyr. The remaining lifetime of an already evolved open cluster (with $\tau_{\rm oc}/T_{\rm diss,0} \gtrsim 0.3$, $\tau_{\rm oc}$ being its current astrophysical age) can be approximated by equation (1) with $\bar{m} \approx 0.75{\rm M}_\odot$, because it has lost most of its lowest-mass stars. The present-day Hyades ($M_{\rm oc} \approx 275{\rm M}_\odot$) will thus dissolve in about 800 Myr. These estimates provide a useful orientation of the life-times of open clusters but are uncertain since they rely on simulations made for significantly more massive cluster models not orbing near the mid-plane of the Galaxy, and since individual open clusters containing $n < 10\,000$ stars follow evolutionary tracks that increasingly diverge from each other for smaller n due to the chaotic nature of small-n dynamics.

The escape process of stars from their cluster is complex. Stars that are *ejected* typically leave the cluster faster than the velocity dispersion after an energetic close encounter with a binary in the cluster. Energy-equipartition-driven *evaporation*, on the other hand, produces stars that have very small velocities relative to the cluster's centre of mass. This two-body-relaxation driven process dominates by far the flux of stars from the cluster at least after the initial binary population has been mostly dynamically processed (Kroupa 1995c). Evaporation can be visualized by noting that at any time the velocity distribution function of stars in the cluster is approximately

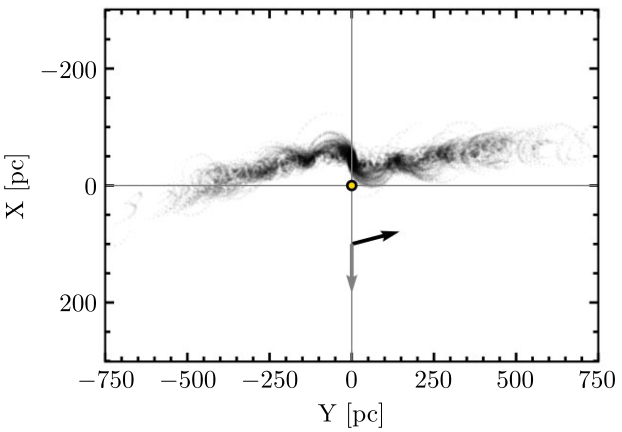

Figure 1. Direct Newtonian n-body computation of a Hyades-like star cluster with initial mass $M_{\rm oc,0} = 1235 M_\odot$ and initial half-mass radius $r_{\rm h0} = 2.6$ pc in a realistic Galactic potential. Stellar particles are shown for a series of snapshots at 620, 625, 630, 635, 640, 645, 650, 655, 660, 665, 670, 675, 680, 685, 690, and 695 Myr in Galactic Cartesian coordinates. The Sun is marked as a yellow point. The grey arrow points to the Galactic centre, and the black arrow is the cluster velocity vector in the corresponding coordinates with the Z-axis pointing towards the North Galactic Pole. The time stacking of snapshots shows the movement of individual stars to and from the Küpper epicyclic overdensities. The realistic star cluster trajectory with excursions out of the Galactic plane does not significantly affect the physical appearance of the tails, while projection effects as seen from the Sun do (model M1 and figure with permission from Jerabkova et al. 2021).

Maxwellian. The high-velocity tail is lost across the práh and is constantly refilled stochastically through two-body relaxation. Even after being formally unbound (having a positive energy), a star can orbit many times around and even through the cluster such that each cluster is surrounded by a 'halo of lingering stars' waiting to exit (Fukushige & Heggie 2000). Whether the star exits near the inner L1 Lagrange point or the outer L2 point is random as it results from the accumulation of many uncorrelated stellar-orbital perturbations (Pflamm-Altenburg et al., in preparation). At galactocentric distances significantly larger than the tidal radius of the cluster, $r_{\rm tid}$ (equation 20 below), the cluster-centric potential is symmetric in Newtonian gravitation and L1 and L2 are equidistantly placed at a distance $r_{\rm tid}$ from the cluster centre-of-mass (CCoM) along the line joining the galactic-centre–CCoM. Due to this symmetry, the leading and trailing tails contain the same number of stars to within Poisson fluctuations. This follows from detailed calculations of stellar orbits (Just et al. 2009; Pflamm-Altenburg et al., in preparation) as well as in the standard linearized treatment of the tidal field (Chumak & Rastorguev 2006a; Ernst et al. 2011). The expected symmetry of the tails is demonstrated in Fig. 1 for a Hyades-like open star cluster.

Since the dispersion of velocities of the evaporated stars is comparable to the velocity dispersion of the cluster, the leading and trailing tidal tails are kinematically cold. Each star that leaves the cluster is on its own rosette orbit about the galaxy. While the rosette orbits belonging to one of the two tails are all next-to-equal, they are phase shifted relative to each other and form a complex superposition pattern of stellar density along the tidal tail. The motion of the stars can be mathematically approximated as epicyclic motions relative to the local guiding centre, which is the CCoM, a detailed analysis being provided by Just et al. (2009). The stars accumulate where their velocities relative to the local circular velocity are slowest and form regularly-spaced *Küpper epicyclic overdensities* along the tails (Küpper, MacLeod & Heggie 2008; Just et al. 2009; Küpper, Lane & Heggie 2012). For clusters not on circular orbits, the same holds except that the form of the tails become more complicated and time-dependent (Küpper et al. 2010). The spacing of the Küpper overdensities is a sensitive function of the gravitational potential of the galaxy and of the mass of the cluster which defines the velocity dispersion of the evaporating stars: a larger escape speed implies a larger velocity dispersion and less-well defined and more distantly-spaced overdensities (Küpper et al. 2015). In Newtonian gravitation, the Küpper overdensities are symmetrically and periodically spaced along the tidal tails. The Küpper overdensities have been detected but not recognized as such around the globular cluster Pal 5 (Odenkirchen et al. 2001, 2003, section 7.3 therein), but have been discussed as such by Erkal, Koposov & Belokurov (2017) [see also Section 5.1]. A fully-dissolved massive-born cluster left the stellar stream GD-1 that has been observed to harbour strong evidence for regularly-spaced Küpper overdensities (Ibata et al. 2020) and Jerabkova et al. (2021) discovered the overdensities for the first time around an open cluster (the Hyades). Apart from being gravitational probes in association with the current mass of the cluster, the tidal tails can test whether the IMF is a probabilistic or an optimal distribution function (Wang & Jerabkova 2021). Once the entire population of stars in the tidal tails is known, then the rate of dissolution of an open cluster can be tested for – can the Newtonian expectation (equation 1) be confirmed?

The open cluster leaves, as its remnant, a high-order multiple stellar system often made of similar-mass stars (de La Fuente Marcos 1998a,b; Angelo et al. 2019), or a dark cluster dominated by stellar remnants (Banerjee & Kroupa 2011). The tidal stream becomes indistinguishable from the Galactic field population as it spreads in length and thickens through perturbations (Chumak & Rastorguev 2006a), a process not yet well understood. Given that embedded clusters loose between 50 to 80 per cent of their stars through gas expulsion (Kroupa & Boily 2002; Brinkmann et al. 2017), it is to be expected that about 20 per cent to a half of all stars would have been released into a galactic field through classical tidal tails II. The spilling-out of stars from their clusters is thus important for defining the stellar phase-space distribution function of a galaxy.

2.2 Extraction from the field and the discovery of the tidal tail asymmetry

Detecting and interpreting the properties of tidal tails is easiest for clusters on circular orbits. By the nature of their origin from the inter-stellar medium of their host galaxy, young (age $\tau_{\rm oc} \lesssim 100$ Myr) to intermediate-aged ($100 \lesssim \tau_{\rm oc}/{\rm Myr} \lesssim 1500$) open clusters are on near-circular orbits within the disc of their galaxy (Chumak & Rastorguev 2006b; Carrera et al. 2022). With the Gaia mission, open star clusters have become prime targets to analyse tidal tails.

The tidal tails around open clusters are difficult to extract from the field population of the Galaxy, since the tail stars are already part of the field population and because they comprise a small fraction of stars in a given volume near an open cluster. Thus, returning to the example of Fig. 1, the open cluster with $M_{\rm oc,0} = 1235 M_\odot$ will have ≈1180 stars in the tails at an age of ≈650 Myr, given the cluster looses 30 per cent of its mass due to stellar evolution and the average stellar mass is $\approx 0.5 M_\odot$. From Fig. 1, each tail can be approximated as a cylinder with a radius of 30 pc and a length of 600 pc corresponding to a volume of 1.7×10^6 pc^3. The stellar number density in the Solar neighbourhood is about one star per pc^3 such that the one-sided tail volume contains about 1.7×10^6 field stars while consisting of 590 ex-cluster stars.

The members of a dissolving cluster that are still close to the cluster have nearly parallel velocity vectors such that their proper

motion directions when plotted as great circles on the celestial sphere intersect at two opposite convergent points. Using this convergent point (CP, Strömberg 1939; de Bruijne 1999; van Leeuwen 2009) method to identify co-moving stars in the *Gaia* DR2, the parts of the tails closest to their clusters have been found around the Hyades (Meingast & Alves 2019; Röser, Schilbach & Goldman 2019), the Praesepe (Röser & Schilbach 2019) and Coma Berenices (Fürnkranz, Meingast & Alves 2019; Tang et al. 2019). These three clusters have similar intermediate-ages (Table 1) such that the stars born in them do not stand-out from the field population in a colour-magnitude diagram. They are close-by to the Sun within 190 pc such that the Gaia data are now allowing the tidal tails to be extracted from the background field population. Using the CP method, the tails of the Hyades (fig. 1 in Meingast & Alves 2019; fig. 3 in Röser et al. 2019), Coma Berenices (fig. 2 in Fürnkranz et al. 2019; fig. 7 in Tang et al. 2019), and the Praesepe (fig. 2 in Röser & Schilbach 2019) have been mapped out to distances of about $d_{\rm cl} \approx 30$–170 pc from their clusters. All leading tails are more populated than the trailing tails. In addition, Bai et al. (2022) report the tidal tails of the open cluster COIN-*Gaia* 13, which is about 513 pc distant, has an age of about 250 Myr and a mass of about $439 M_\odot$. Its leading tail also appears to contain more stars than its trailing tail (their fig. 4). Given the importance of mapping out tidal tails for the fundamental questions noted above, it would be desirable to trace the tails to their end tips. But the CP method cannot pick-up stars in the extended tails because their space motions differ systematically from the CCoM.

The new *compact convergent point method* (CCP) introduced by Jerabkova et al. (2021) uses the information that a tidal tail is a causally correlated but extended kinematical structure. The Jerabkova-CCP method uses direct n-body computations of each open cluster to quantify a transformation which maps the extended tidal tail phase-space structure into a compact configuration for stars that belong to the structure. This allows extraction of strong candidates from the background field population even to the tips of the tidal tails. The Küpper overdensities were found for the first time for an open cluster using this method (Jerabkova et al. 2021). The CCP method is not very sensitive to the exact dynamical age of the so-designed model since the tails develop slowly and on a much longer time-scale than the present-day half-mass crossing time in the cluster (being about 10 Myr for the Hyades).

How confidently are the extended tidal tails mapped out using the new CCP method? The CCP method uses the older CP method as a benchmark. The CP method is essentially a zeroth-order approximation as it assumes the tail stars to share the same space motion as the bulk of the cluster. The CCP method relies on an n-body model of the star cluster to have been evolved to its present-day position and velocity such that the calculated tidal tails are used to filter out from the Gaia data, those stars that match, within a tolerance, the phase-space occupied by the model tails. In this procedure the zeroth order approximation in the model needs to match the CP-derived tidal tails exactly, therewith enforcing a strict anchor for the CCP method. Due to uncertainties in the orbit determination the final model needs to be adjusted in position and velocity (the same shift in 6D space for all stars in the model) to agree with the real cluster position. This adjusted model is then compared to the tidal tails recovered with the CP method. The details are documented in Jerabkova et al. (2021). It will be important to continue testing the CCP method with the newer *Gaia* DR3 and DR4 including complementary data (e.g. radial velocities, stellar spin rates, chemical tagging) and further n-body models to more comprehensively quantify the degree of uncertainty, bias, and large-scale completeness in the derived tidal tails.

The CCP method has been applied to the the similarly-aged (600−800 Myr) open clusters Hyades (Jerabkova et al. 2021), Praesepe and Coma Berenices (Jerabkova et al., in preparation). The extracted tidal tails are shown in Fig. 2. Boffin et al. (2022) applied a slightly amended Jerabkova-CCP method to the ≈1.75 Gyr old open cluster NGC 752, finding the tails to be extended for at least 260 pc from tip to tip and the leading tail to also contain more stars than the trailing one.

In summary, it is noteworthy that all five open clusters (Hyades, Praesepe, Coma Berenices, COIN-*Gaia* 13 and NGC 752) which have tail data have the leading tail more populated than the trailing tail within a cluster-centric distance of $d_{\rm cl} \approx 50$ pc. To avoid the halo of unbound stars lingering around each cluster and numerical resolution contraints, we here only study the tail asymmetry in the distance range $50 < d_{\rm cl}/{\rm pc} < 200$ for the three similarly-aged clusters Hyades, Praesepe and Coma Berenices with corresponding data (Section 2.3), but the caveat be added that the results on Praesepe and Coma Ber are preliminary. The NGC 752 cluster is much older, further from us and the tail data only reach to $d_{\rm cl} \approx 130$ pc, such that this cluster is not currently accessible to the MOND models with the available approximative means, as discussed below.

2.3 Properties of the Hyades, Praesepe, Coma Berenices, NGC 752

In order to take the first step towards constraining the possible origin for the observed tail asymmetry evident in the previous work using the CP method (Section 2.2) and the new results applying the CCP method (Fig. 2), the known data on the four clusters with CCP-extracted tail data are collated in Table 1.

The table lists the positions and velocities of the four clusters, and also different estimates for their orbital properties in the Galactic potential. The true orbits are somewhat uncertain because the Galactic potential is uncertain. Two methods are applied to estimate the orbital eccentricity for each cluster: The first method (Pflamm-Altenburg et al., in preparation) assumes the Galactic potential as given in Allen & Santillan (1991). Each cluster is integrated backwards with a time-symmetric Hermite method (Kokubo, Yoshinaga & Makino 1998) for the nominal age as given in Table 1. For this purpose, the observed postions and velocities of the star clusters in the equatorial system are converted into a Galactic inertial rest frame using a Solar position of (−8300, 0, 27 pc) and a velocity of 11.1, 232.24, 7.25 km s^{-1}, as in Jerabkova et al. (2021). This provides the most recent peri- and apo-galacticon distances, $R_{\rm peri}$, $R_{\rm apo}$, respectively, and the maximum excursion from the Galactic mid-plane, $Z_{\rm max}$. The orbital eccentricity, e, follows from

$$e = (R_{\rm apo} - R_{\rm peri})/(R_{\rm apo} + R_{\rm peri}). \quad (2)$$

An alternative estimate of the orbital eccentricity, $e_{\rm snap}$, follows from the current position and velocity data of the cluster, i.e. from the present-day snapshot. The method assumes the Galaxy has a flat rotation curve, the details being provided in Appendix A.

In order to focus on the parts of the tidal tails closest to the clusters but sufficiently far to avoid the halo of lingering stars (Section 2.1), and to be outside the tidal radius (equation 20) of the models developed below, the number of stars is counted in the leading and trailing tails in the distance range 50–200 pc from the clusters. That the Küpper overdensities are located within this distance in the real open clusters (e.g. the first Küpper overdensity is expected to be, in Newtonian-models at about $d_{\rm cl} = 130$ pc for the Hyades, Fig. 1), does not affect the ratio since the stars drift along the tail and through the overdensity which only very slowly

Table 1. The present-day cluster parameters for the Hyades, Praesepe, Coma Berenices, and NGC 752. These are from top to bottom: alternative name, right ascension (RA), declination (DEC), both epoch J2000), and parallax, ϖ of the cluster's centre, it's distance from the Sun, d, and proper motion in RA, $\mu_{\alpha*}$ in DEC, μ_δ, and line of sight velocity, $v_{\rm los}$. Assuming the Galactic potential of Allen & Santillan (1991) and the Solar position ($R_{\rm GC\odot} = 8300$ pc) and velocity vector as given in Jerabkova et al. (2021): the velocity components $V_{\rm X}$, $V_{\rm Y}$, $V_{\rm Z}$ and the total velocity or speed, $v_{\rm tot}$, current Galactocentric distance, R, its last apo-, $R_{\rm apo}$, and last peri-galactic distance, $R_{\rm peri}$, the last maximum orbital excursion away from the Galactic midplane, $Z_{\rm max}$, the orbital eccentricities, e (equation 2, obtained by full orbit integration in the Galactic potential from Allen & Santillan 1991), $e_{\rm snap}$ (app) (obtained from the current postion and velocity vector and the approximative solution for a flat rotation curve with $v_{\rm circ} = 220\,{\rm km\,s^{-1}}$, see Appendix A), and $e_{\rm snap}$ (num) (obtained from the current postion and velocity vector and the Newton–Raphson solution, see Appendix A), (Section 2.3), and the sign of the Galactocentric radial velocity component (+1 = receding, −1 = approaching the Galactic centre). The constrained age range is given by $\tau_{\rm oc}$ and the stellar mass is $M_{\rm oc}$ within the tidal radius $r_{\rm tid}$ (equation 20). The half-mass radius is $r_{\rm h}$. The MOND radius (equation 13) is $r_{\rm M}$. The number of stars found using the Jerabkova-CCP method in the cluster and in the tidal tail II are, respectively, $N_{\rm tot}$, $N_{\rm tidal}$. $N_{\rm lead}$, and $N_{\rm trail}$ stars and in the leading and trailing tails, respectively. Within the distance 50–200 pc, $N_{\rm lead}$ (50−200 pc) of these stars are in the leading tail and $N_{\rm trail}$ (5−200 pc) in the trailing tail, the ratio of these being given by $q_{\rm 50-200\,pc}$. The following numbers assume the cluster has a present-day stellar mass $M_{\rm oc}$: The internal acceleration is $a_{\rm int}$ (equation 9), the external acceleration (equation 8) is $a_{\rm ext,kin} = a_{\rm bulge} + a_{\rm disc} + a_{\rm halo}$ (adopting here $v_{\rm circ} = 250\,{\rm km\,s^{-1}}$ in equation 8; this includes the total gravitational acceleration in Milgromian or equivalently in Newtonian gravitation with the dark matter halo such that the rotation curve is as shown in Fig. 4), and $a_{\rm ext,bary} = a_{\rm bulge} + a_{\rm disc}$ (i.e. only Newtonian-baryonic without the phantom dark matter halo, Fig. 4). The line-of-sight (1D) velocity dispersion in Milgromian gravitation is $\sigma_{\rm M,iso,los}$ assuming the cluster is isolated (equation 10) and $\sigma_{\rm M,ef,los}$ assuming it is situated within an EF given by $a_{\rm ext,kin}$ (equation 11). The Newtonian line-of-light (1D) velocity dispersion is equation (11) with $G = G_{\rm eff}$.

Name	Hyades	Praesepe	Coma Berenices	NGC 752
alt. names	Mel 25	Mel 88, M44, NGC 2632	Mel 111	Mel 12
RA(J2000)	04h 31min 56.4s (1)	08h 40min 12.9s (3)	12h 25min 06s (4)	01h 56min 39.21s (11)
DEC(J2000)	17.012° (1)	19.621 (3)	26.100° (4)	37.795° (11)
ϖ/mas	21.052 (2)	5.361 (3)	11.640 (2)	2.281 (11)
d/pc	47.5	186.5	85.9	438
$\mu_{\alpha*}$/mas yr^{-1}	101.005 (2)	−36.090 (3)	−12.111 (2)	9.77 (11)
μ_δ/mas yr^{-1}	−28.490 (2)	−12.919 (3)	−8.996 (2)	−11.78 (11)
$v_{\rm los}$/km s^{-1}	39.96 (2)	35.84 (2)	−0.52 (2)	8.2 (11)
($V_{\rm X}$, $V_{\rm Y}$, $V_{\rm Z}$)/pc Myr^{-1}	(−32.01, 212.37, 6.13)	(−32.56, 216.53, −2.74)	(8.92, 231.78, 6.29)	(−8.37, 221.02, −13.10)
$V_{\rm tot}$/pc Myr^{-1}	220.3	219.0	232.0	221.6
(X, Y, Z)/pc	(−8344.44, 0.06, 10.22)	(−8441.57, −68.90, 127.03)	(−8306.71, −5.91, 112.44)	(−8294.05, 275.07, −158.408)
R/pc	8344.4	8441.9	8306.7	8298.6
$R_{\rm apo}$/pc	9013.4	9060.4	8937.4	8604.7
$R_{\rm peri}$/pc	7311.7	7375.0	8217.7	7746.8
$Z_{\rm max}$/pc	−63.8	130.8	−136.0	213.4
e	0.104	0.103	0.042	0.052
$e_{\rm snap}$(app)	0.115	0.114	0.038	0.0567
$e_{\rm snap}$(num)	0.105	0.103	0.041	0.0538
d$R_{\rm GC}$/dt (sign)	+1	+1	−1	+1
$\tau_{\rm oc}$/Myr	580–720 (10)	708–832 (6)	700–800 (9)	≈1.75 (11)
$M_{\rm oc}$/M$_\odot$	275 (5)	311 (6)	112 (8)	379 (11)
$r_{\rm h}$/pc	4.1 (5)	4.8 (6)	3.5 (7)	5.3 (11)
$r_{\rm tid}$/pc	9.0 (5)	10.77 (6)	6.9 (9)	9.4 (11)
$r_{\rm M}$/pc	0.57	0.61	0.36	0.67
$N_{\rm tot}$	862 (1)	1170 (12)	730 (12)	640 (11)
$N_{\rm tidal}$	541 (1)	833 (12)	640 (12)	298 (11)
$N_{\rm lead}$	351 (1)	384 (12)	348 (12)	163 (11)
$N_{\rm trail}$	190 (1)	449 (12)	292 (12)	135 (11)
$N_{\rm lead}(50–\gamma$ pc)	162 ($\gamma = 200$)	87 ($\gamma = 200$)	133($\gamma = 200$)	56($\gamma = 130$)
$N_{\rm trail}(50–\gamma$ pc)	64($\gamma = 200$)	140($\gamma = 200$)	111($\gamma = 200$)	43($\gamma = 130$)
$q_{50-\gamma\,\rm pc}$	$2.53 \pm 0.37(\gamma = 200)$	$0.62 \pm 0.08(\gamma = 200)$	$1.20 \pm 0.15(\gamma = 200)$	$1.30 \pm 0.24(\gamma = 130)$
$a_{\rm int}$/pc Myr^{-2}	0.037	0.030	0.021	0.030
$a_{\rm ext,kin}$/pc Myr^{-2}	7.5	7.4	7.5	7.5
$a_{\rm ext,bary}$/pc Myr^{-2}	4.1	4.1	4.2	4.3
$\sigma_{\rm M,iso,los}$/km s^{-1}	0.69	0.71	0.55	0.75
$\sigma_{\rm M,ef,los}$/km s^{-1}	0.29	0.28	0.20	0.28
$\sigma_{\rm N,los}$/km s^{-1}	0.22	0.22	0.15	0.23

Notes. *References*: (1) Jerabkova et al. (2021), (2) Gaia Collaboration (2018), (3) Cantat-Gaudin et al. (2018), (4) Dias et al. (2014), (5) Röser et al. (2011), (6) Röser & Schilbach (2019), (7) Krause et al. (2016), (8) Kraus & Hillenbrand (2007), (9) Tang et al. (2019), (10) Röser et al. (2019), (11) Boffin et al. (2022), (12) Jerabkova et al. (in preparation).

shifts closer to the cluster as the cluster evaporates (Section 2.1). The number ratio of leading to trailing tail stars in the distance range 50–200 pc, $q_{\rm 50-200\,pc}$ is listed in Table 1. The Hyades and NGC 752 show a similar asymmetry with the leading tail containing, respectively, 2.53 ± 0.37 and 1.30 ± 0.24 times as many stars than the trailing tail between, respectively, $d_{\rm cl} = 50$ and 200 pc and 50 to 130 pc from the CCoM. This is in 6.5 sigma tension for the former with Newtonian models assuming the Hyades orbits in a smooth axisymmetric

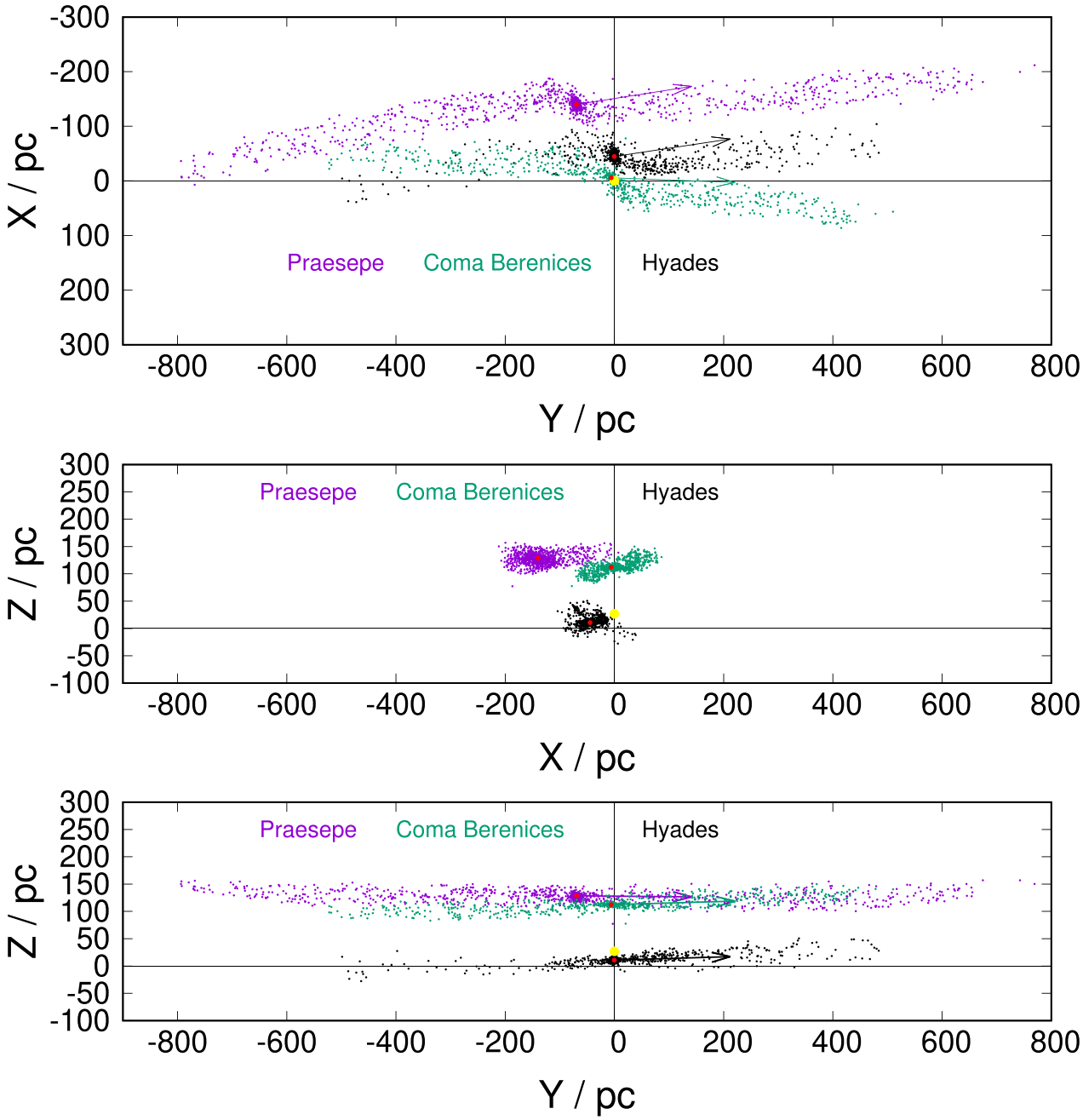

Figure 2. The classical tidal tails II extracted from the *Gaia* eDR3 using the CCP method by Jerabkova et al. (2021) for the Hyades, and for Coma Berenices and Praesepe by Jerabkova et al. (in preparation) in the three projections in Galactic Cartesian coordinates. The Galactic centre is towards positive X and Galactic rotation points towards positive Y. The coordinate system is anchored at $(X, Y, Z) = (0, 0, 0)$ pc and the Sun is the filled yellow circle at $(0, 0, +27)$ pc. The centre of each cluster is indicated by the filled red dot. Note that Coma Berenices lies almost directly above the Sun towards the Galactic north pole. The arrows show the full orbital and peculiar motions of each cluster with a length corresponding to $V_{X,Y,Z}$ in Table 1. The middle panel does not show the velocity arrows as these are directed mostly into the plane.

Allen & Santillan (1991) Galactic potential (Pflamm-Altenburg et al., in preparation).

The observed degree of asymmetry for the Hyades can be obtained through an on-going encounter with a dark lump of mass $\approx 10^7 M_\odot$ (Jerabkova et al. 2021). This is a reasonable hypothesis to explain the asymmetry for one cluster. But such a dark lump is not observed in the form of a molecular cloud (fig. 11 in Miville-Deschênes et al. 2017; the Sun and Hyades cluster lying within the local cavity of low density, high-temperature plasma of radius ≈ 150 pc, Zucker et al. 2022), and if it were a dark-matter subhalo, a similar type of encounter with a similar geometry and timing would have had to have happened also for NGC 752 simultaneously at the present time in the immediate vicinity of the Sun. This is unlikely (with dark matter not having been detected and probably not existing Kroupa 2015; Roshan et al. 2021; Asencio et al. 2022). With no corresponding perturbation in the local phase-space distribution of field stars having been reported, a perturbation being the origin for the observed asymmetries is not further considered in the following.

3 MILGROMIAN GRAVITATION AND OPEN STAR CLUSTERS

Given that the observed asymmetry between the leading and trailing tails of open clusters appears to be difficult to be explained in Newtonian gravitation, the asymmetry problem is now studied in a modern non-relativistic theory of gravitation. This section contains a brief introduction to Milgromian Dynamics (MOND), the revised Poisson equation (Section 3.1), its implication for the equipotential surface around a gravitating body and for open star clusters (Section 3.2).

3.1 The generalized Poisson equation and the PoR code

The standard (Newtonian) Poisson equation,

$$\vec{\nabla} \cdot [\vec{\nabla}\phi_{\rm N}] = 4\pi G \rho_{\rm b}, \tag{3}$$

allows the position vector, $\vec{R}$, dependent phase-space baryonic mass density, $\rho_{\rm b}(\vec{R})$, of the cluster plus hosting galaxy to generate the Newtonian potential, $\phi_{\rm N}(\vec{R})$, the negative gradient of which provides the acceleration at $\vec{R}$.

Milgrom (1983) extended the non-relativistic formulation of Newton/Einstein beyond the Solar system by invoking dynamics data, which had become available for disc galaxies a few years prior to 1983, but decades after Einstein (1916). Milgrom (1983) conjectured that gravitational dynamics changes to an effectively stronger form when the gradient of the potential falls below a critical value,[2] $a_0 \approx 3.8\,{\rm pc\,Myr^{-2}}$, which appears to be a constant in the local Universe but may be related to an energy scale of the vacuum and to the expansion rate of the Universe (for reviews see Sanders & McGaugh 2002; Scarpa 2006; Sanders 2007, 2015; Famaey & McGaugh 2012; Milgrom 2014; Trippe 2014; Merritt 2020; Banik & Zhao 2022, the latter containing discussions of relativistic formulations that are consistent both with the cosmic microwave background (CMB) and the speed of gravitational waves.).[3]

Energy- and momentum conserving time-integrable equations of motion of non-relativistic gravitating bodies became available through the discovery of 'a quadratic Lagrangian' (AQUAL) as a generalization of the non-relativistic Newtonian Lagrangian by Bekenstein & Milgrom (1984). This lead to the non-linear AQUAL-MOND Poisson equation that is related to the well-known p-Laplace operator,

$$\vec{\nabla} \cdot \left[\mu \left(\frac{|\vec{\nabla}\Phi|}{a_0} \right) \vec{\nabla}\Phi \right] = 4\,\pi\, G\, \rho_{\rm b}, \tag{4}$$

where $\mu(x) \rightarrow 1$ for $x = |\vec{\nabla}\Phi|/a_0 \rightarrow \infty$ and $\mu(x) \rightarrow x$ for $x \rightarrow 0$, the transition function, $\mu(x)$, being derivable from the quantum vacuum (Milgrom 1999). Observational data show the value of Milgrom's constant a_0 to be $0.9 \times 10^{-10} < a_0/({\rm m/s^2}) < 1.5 \times 10^{-10}$ (Gentile, Famaey & de Blok 2011, i.e. $a_0 \approx 3.8\,{\rm pc\,Myr^{-2}}$).

Equation (4) allows $\rho_{\rm b}(\vec{R})$ to generate the full Milgromian potential, $\Phi(\vec{R})$, the negative gradient of which provides the acceleration as in standard gravitation. Solving this generalized Poisson equation in regions of high acceleration recovers the Newtonian potential ($\mu = 1$ retrieving equation 3), while in low-acceleration regions where the gradient of the potential is smaller than a_0, the acceleration comes out to be stronger. As a consequence of the non-linear nature of the generalized Poisson equation, the boundary conditions differ to those in Newtonian gravitation and Φ depends on the external acceleration from the mass distribution in the neighbourhood. The rotation curve of a non-isolated disc galaxy of baryonic mass $M_{\rm b}$ within an external field (EF) will decrease with increasing galactocentric distance, while it is constant for an isolated (no EF) disc galaxy of the same baryonic mass (Haghi et al. 2016; Chae et al. 2020). In other words, the isolated galaxy has a larger effective-Newtonian gravitational mass,[4] $M_{\rm grav,iso}$, than the non-isolated galaxy ($M_{\rm grav,niso}$), generating around itself at large $|\vec{R}|$ a spherical logarithmic potential $\Phi(\vec{R})$. In both cases though, $M_{\rm grav} > M_{\rm b}$ with $M_{\rm grav,iso} > M_{\rm grav,niso}$. This effect on Φ is called the 'external field effect' (EFE) and causes self-gravitating systems to become effectively Newtonian when the external acceleration is stronger than the internal acceleration. The EFE has been observationally confirmed with more than $5\,\sigma$ confidence (Chae et al. 2020, 2021, see also Haghi et al. 2016; Hees et al. 2016). The external field is also present in Newtonian gravitation but because the potentials add linearly, it can be subtracted and has no influence on the internal dynamics of a self-gravitating system falling within the external field. In Milgromian gravitation on the other hand, due to the generalized Poisson equation (equation 4), the internal dynamics depends on this external field by non-linearly changing the effective-Newtonian gravitational masses of the constituents in dependence of their location within the system. The strong equivalence principle is thus not obeyed in Milgromian gravitation and the internal physics of falling bodies depend on their gravitational environment. Oria et al. (2021) discuss the EFE in the context of the mass distribution in the Local Cosmological Volume.

Equation (4) can be readily solved using well-known methods if the distribution of matter, $\rho_{\rm b}$, can be approximated as a continuum, which is equivalent to the system in question being 'collision-less', or synonymously, the system having a two-body relaxation time longer than a Hubble time (Kroupa 1998; Forbes & Kroupa 2011; Misgeld & Hilker 2011). Galaxies are collision-less systems such that particle-mesh-grid-based methods can be used to calculate the flow of phase-space mass density. In Newtonian gravitation, the distribution of discrete particles can be combined in discrete spatial grid cells in which the mass density, $\rho_{\rm b}(\vec{R})$, is thusly defined. The standard Newtonian potential, $\phi_{\rm N}(\vec{R})$, can thereupon be computed by solving the Poisson equation (equation 3) on the discrete grid using different efficient techniques. Once the potential is known in each cell, the Newtonian acceleration, $\vec{a}(\vec{R},t) = -\vec{\nabla}\phi_{\rm N}(\vec{R},t)$, can be computed for each grid point and thus for each particle at its location by interpolation, to finally advance each particle through position-velocity space by one step in time. This process is repeated after each time-step to move a Newtonian system forwards in time.

A collision-less n-body code based on solving equation (4) on a spherical-coordinate grid for isolated systems was developed by Londrillo & Nipoti (2009). This code has been applied to a number of star-cluster-relevant problems including the EFE (Haghi et al. 2009; Sollima et al. 2012a; Wu & Kroupa 2013, 2018, 2019) but is not usable here as the spherically-symmetrical grid does not allow the tidal tails to be followed in sufficient detail.

[2]Throughout this text and depending on the context, the unit for velocity is ${\rm pc\,Myr^{-1}}$ or ${\rm km\,s^{-1}}$, noting that $1\,{\rm pc\,Myr^{-1}} = 0.9778\,{\rm km\,s^{-1}} \approx 1\,{\rm km\,s^{-1}}$ to a sufficient approximation.

[3]The interpretation of MOND as a generalized-inertia theory is an alternative to interpreting MOND as a theory of gravitation, and is related to Mach's principle, but has not been developed as a computable theory (Milgrom 2014; Milgrom 2022). Loeb (2022b) points out an implication for space travel.

[4]Note that in MOND there is no 'gravitating mass' beyond the mass contributed by the particles in the standard model of particle physics, and 'effective-Newtonian gravitational mass' is not a true gravitating mass but a mathematical formulation assuming Newtonian gravitation.

The computational burden for calculating $\Phi(\vec{R})$ has been reduced significantly by the development of a quasi-linear formulation of MOND (QUMOND, Milgrom 2010), which requires to solve only linear differential equations, with one additional algebraic calculation step, allowing a quick and efficient implementation in existing particle-mesh *n*-body codes. The generalized Poisson equation in QUMOND is

$$\nabla^2\Phi(\vec{R}) = 4\pi G\rho_{\rm b}(\vec{R}) + \vec{\nabla}\cdot[\widetilde{\nu}(|\vec{\nabla}\phi_{\rm N}|/a_0)\vec{\nabla}\phi_{\rm N}(\vec{R})], \quad (5)$$

where $\widetilde{\nu}(y) \rightarrow 0$ for $y \gg 1$ (Newtonian regime) and $\widetilde{\nu}(y) \rightarrow y^{-1/2}$ for $y \ll 1$ (Milgromian regime; note that μ and $\widetilde{\nu}$ are algebraically related, see Famaey & McGaugh 2012; Milgrom 2014) with $y = |\vec{\nabla}\phi_{\rm N}|/a_0$. This means that the total Milgromian gravitational potential, $\Phi = \phi_{\rm N} + \Phi_{\rm ph}$, can be divided into a Newtonian part, $\phi_{\rm N}$, and an additional phantom part, $\Phi_{\rm ph}$. The matter density distribution, $\rho_{\rm ph}(\vec{R})$, that would, in Newtonian gravitation, yield the additional potential, $\Phi_{\rm ph}(\vec{R})$, and therefore obeys $\nabla^2\Phi_{\rm ph}(\vec{R}) = 4\pi G\rho_{\rm ph}(\vec{R})$, is known in the Milgromian context as the phantom dark matter (PDM) density,

$$\rho_{\rm ph}(\vec{R}) = \frac{1}{4\pi G}\vec{\nabla}\cdot[\widetilde{\nu}(|\vec{\nabla}\phi_{\rm N}(\vec{R})|/a_0)\vec{\nabla}\phi_{\rm N}(\vec{R})]. \quad (6)$$

PDM is not real matter but a mathematical description helping to compute the additional gravity in Milgrom's formulation, giving it an analogy in Newtonian dynamics. In the context of the Local Cosmological Volume, Oria et al. (2021), calculate regions with $\rho_{\rm ph} < 0$ that may be identifiable with weak lensing surveys. This phantom mass density does not take part in the time-integration and does not introduce Chandrasekhar dynamical friction into the system. In the above terminology, $M_{\rm oc,grav} = M_{\rm oc} + M_{\rm oc,ph} > M_{\rm oc}$. The PDM density that would source the Milgromian force field in Newtonian gravity can thus be calculated directly from the known baryonic density distribution, $\rho_{\rm b}(\vec{R})$. A grid-based scheme can be used to calculate $\rho_{\rm ph}(\vec{R})$ from the discrete Newtonian potential, $\phi_{\rm N}^{\rm i,j,k}$ (see equation 35 in Famaey & McGaugh 2012, and also Milgrom 2010; Gentile et al. 2011; Lüghausen et al. 2013; Lüghausen, Famaey & Kroupa 2014, Lüghausen, Famaey & Kroupa 2015 and Oria et al. 2021). Once this source of additional acceleration is known, the total (Milgromian) potential can be computed readily using the Poisson solver already implemented in the grid-based code.

The above QUMOND technique was implemented independently by Lüghausen et al. (2015) and Candlish, Smith & Fellhauer (2015) into the existing RAMSES code developed for Newtonian gravitation by Teyssier (2002). RAMSES employs an adaptively refined grid structure in Cartesian coordinates such that regions of higher density are automatically resolved with a higher resolution. It computes the Newtonian potential $\phi_{\rm N}(\vec{R})$ from the given baryonic mass-density distribution, $\rho_{\rm b}(\vec{R})$, i.e. it solves the discrete Poisson equation (equation 3). In the Phantom of Ramses (PoR) code, Lüghausen et al. (2015) added a subroutine, which on the adaptive grid computes the PDM density from the Newtonian potential (equation 6) and adds the (mathematical) DM-equivalent density to the baryonic one. The Poisson equation is then solved again to obtain the Milgromian potential, $\Phi = \phi_{\rm N} + \Phi_{\rm ph}$, i.e. the 'true' (Milgromian) potential, which is used to integrate the stellar particles in time through space (each stellar particle experiencing the acceleration $\vec{a}_{\rm star}(\vec{R}) = -\vec{\nabla}\Phi(\vec{R})$) and to solve the Euler equations for the dynamics of the gas.

Although any interpolating function can in principle be chosen, the PoR code adopts as the default interpolating function

$$\widetilde{\nu}(y) = -\frac{1}{2} + \left(\frac{1}{4} + \frac{1}{y}\right)^{\frac{1}{2}}, \quad (7)$$

and has already been used on a number of problems (for the manual and description see Nagesh et al. 2021).

By employing a Cartesian grid, the PoR code is suited to study the leakage of stellar particles across a cluster's práh and to follow the tidal tails with an application to this problem by Thomas et al. (2018) accounting for the observed length asymmetry between the leading and trailing tail of the globular cluster Pal 5.

3.2 Open clusters

3.2.1 General comments

In contrast to galaxies, open star clusters are 'collisional' systems in which the two-body relaxation time is significantly shorter than one Hubble time, $\tau_{\rm H}$, i.e. in which the thrive towards energy-equipartition plays a decisive evolutionary role. For open clusters, the dissolution time (equation 1) is shorter than the Hubble time, $T_{\rm diss} < \tau_{\rm H}$. The evolution of an open cluster therefore needs to be calculated through the direct star-by-star accelerations. Due to the simplifying linear-additivity of forces in Newtonian gravitation, advanced computer codes have been developed for this purpose (Aarseth 1999; Aarseth, Tout & Mardling 2008; Aarseth 2010; Portegies Zwart et al. 2013; Wang et al. 2020). With these codes, it has been possible to solve the problem why the binary-star fraction in the Galactic field is 50 per cent, while it is about 100 per cent in star-forming regions (Kroupa 1995a,b; Marks & Kroupa 2011), to infer that the Pleiades cluster formed from a binary-rich Orion Nebula Cluster-like precursor (Kroupa et al. 2001) with multiple stellar populations (Wang, Kroupa & Jerabkova 2019), and how intermediate-massive clusters are affected by a realistic high-initial binary population (Wang, Tanikawa & Fujii 2022). But at the present there are no codes that allow this to be done in Milgromian gravitation.

3.2.2 Open clusters in Milgromian gravitation: the phantom extends the práh

Despite it not being possible at this time to do exact calculations of the dynamical evolution of open clusters in Milgromian gravitation, some estimates are possible, given the existing tools.

An open cluster (or satellite galaxy) at a position vector $\vec{R}$ in the Galactocentric reference frame will be subject to an EF,

$$\vec{a}_{\rm ext,kin} = -\frac{v_{\rm circ}^2}{R}\frac{\vec{R}}{R} \approx -G\frac{M_{\rm MW,grav}(R)}{R^3}\vec{R}, \quad (8)$$

where $M_{\rm MW,grav}(R)$ is the effective-Newtonian gravitational mass of the here-assumed-spherical Galaxy within $\vec{R}$, $M_{\rm MW,grav}(R)$ being obtained from dynamical tracers, such as the rotation curve within R. For example, for the Hyades $|\vec{a}_{\rm ext,kin}| \equiv a_{\rm ext,kin} \approx 7.5\,{\rm pc\,Myr^{-2}} \approx 2.0\,a_0$ ($M_{\rm MW,grav} \approx 1.15\times10^{11}{\rm M}_\odot$, $R \approx 8300\,{\rm pc}$ for circular velocity $v_{\rm circ} = 250\,{\rm pc\,Myr^{-1}}$). As a consequence, the dynamics of open star clusters is much richer than in Newtonian gravitation, since, for example, a star cluster will change its self-gravitational energy and thus its two-body relaxational behaviour as it orbits within a galaxy due to the changing external field from the galaxy (Wu & Kroupa 2013). In Table 1 $a_{\rm ext,kin}$ (equation 8) and $a_{\rm ext,bary}$ are documented for the four open clusters, referring to the EF generated by the total gravitating mass ($M_{\rm MW,grav}$, baryonic plus dark matter for the rotation curve as shown in Fig. 4) and only the Newtonian acceleration through the baryons (replacing $M_{\rm MW,grav}$ in equation (8) by $M_{\rm bulge+disc}$), respectively.

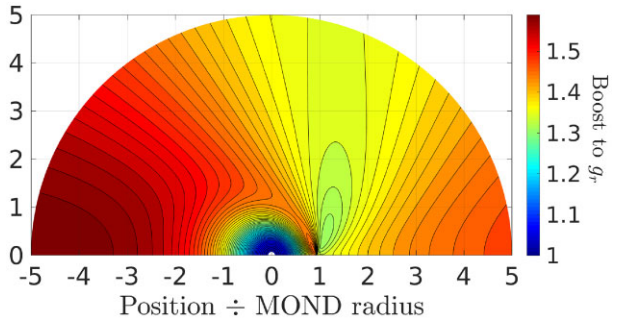

Figure 3. The radial acceleration-field around an open cluster, approximated here as a point-mass, is enhanced in Milgromian dynamics, as shown by the 'boost' of the radial component of the gravitational acceleration above the Newtonian expectation. Positions on the x, y-axes are in units of the MOND radius $r_{\rm M}$ (equation 13). The Galactic centre is in the direction of positive x and is 8.3 kpc distant and a constant $a_{\rm ext} = a_0$ (equation 8) pointing towards the Galactic centre is assumed across the cluster. The distance orthogonal to this direction, which is the direction of a circular orbit, is shown on the y-axis. Thus, a star on the far side of the cluster at $x = -4$, $y = 0$ experiences a radial acceleration towards the cluster centre at $x = 0$, $y = 0$, which is about 15 per cent larger than a star at $x = 4$, $y = 0$ on the near-side of the cluster. For numerical reasons, accurate results within $\approx 0.1 r_{\rm M}$ are not possible, a region where Newtonian and Milgromian gravity should be almost identical (for details on the calculation, see Banik & Kroupa 2019b; reproduced with kind permission from Banik & Kroupa 2019b).

The open clusters in Table 1 have an internal Newtonian acceleration (Haghi et al. 2019)

$$a_{\rm int} = G\,\frac{M_{\rm oc}}{2\,r_{\rm h}^2} \ll a_0. \tag{9}$$

As already noted by Milgrom (1983), the open clusters in the Solar neighbourhood are in the EF dominated regime with $a_{\rm int} \ll a_{\rm ext,kin} \approx 2\,a_0$. Their internal dynamics can therefore roughly be approximated by Newtonian gravitation with a larger effective Newtonian constant (equation 12 below).

Because the effective-Newtonian gravitational mass of an open cluster is larger than its mass in stars, $M_{\rm oc,grav} > M_{\rm oc}$,[5] the escape speed from the open cluster is increased in comparison to the Newtonian/Einsteinian case, where $M_{\rm oc,grav} = M_{\rm oc}$. Detailed calculations have shown the zero-equipotential surface around the cluster to be lopsided about the position of the density maximum of the cluster due to the non-linearity of the generalized Poisson equation (Fig. 3 below, Wu et al. 2010, 2017; Thomas et al. 2018), such that the escape of stars may be directionally dependent. But also the internal stellar-dynamical exchanges differ from Newtonian gravitation. One can visualize this problem as follows: An isolated star A of mass $m_{\rm A}$ generates around itself a logarithmic Milgromian potential $\Phi_{\rm A}$ with a gravitating phantom mass, $m_{\rm ph,A} \gg m_{\rm A}$, at large distances. Placing another star B near it reduces $m_{\rm phA}$ by virtue of the EF from star B. A third star C will thus experience an acceleration from star A and B which is not the vectorial sum of their Newtonian accelerations and with a magnitude and direction which depends on the separation of A and B. Gravitational dynamics thus has parallels to quark dynamics, as has been pointed out by Bekenstein & Milgrom (1984). The larger effective-Newtonian gravitational masses of the stars lead to stronger two-body relaxation while the larger effective-Newtonian gravitational masses of the whole cluster increases the barrier for escape. It is therefore unclear for the time being how real open clusters evolve in Milgromian gravitation.

The isolated open cluster would have a 1D (line-of-sight) velocity dispersion (assuming spherical symmetry and an isotropic velocity distribution function)

$$\sigma_{\rm M,iso,los} \approx \left(\frac{4}{81}\,G\,a_0\,M_{\rm oc}\right)^{\frac{1}{4}}, \tag{10}$$

with the 1D velocity dispersion of an EF-dominated open cluster being

$$\sigma_{\rm M,ef,los} \approx 3^{-1/2}\left(\frac{G'M'}{2\,r_{\rm h}}\right)^{\frac{1}{2}}. \tag{11}$$

In this equation we can write either

$$G' = G_{\rm eff} = \frac{\rm G}{\mu({\rm x})} \quad \text{with} \quad M' = M_{\rm oc},$$
$$\text{or}$$
$$G' = G \quad \text{with} \quad M' = M_{\rm oc,grav} = \frac{\rm M_{oc}}{\mu({\rm x})}, \tag{12}$$

being, respectively, the boosted gravitational constant or the effective-Newtonian gravitational mass of the open cluster with $\mu(x)$ being given by equation (17) below (e.g. McGaugh & Milgrom 2013).[6] For the open clusters in Table 1, either $G_{\rm eff} \approx 1.5\,G$ or $M_{\rm oc,grav} \approx 1.5\,M_{\rm oc}$.

Table 1 provides estimates of $a_{\rm int}$ and of $\sigma_{\rm M,iso,los}$, assuming the clusters are isolated, and of $\sigma_{\rm M,ef,los}$ using the above analytic estimate. The variation of $a_{\rm ext,bary}$ and $a_{\rm ext;kin}$ as an open cluster oscillates through the Galactic mid-plane adds to the complexity, but these variations are of second order only.

The data in Table 1 show that open clusters in isolation would be significantly supervirial by a factor of 2.3–3.4 relative to the Newtonian expectation. This is indeed the case in observations and is equivalent to the Milgromian expectation that $M_{\rm grav,oc} > M_{\rm oc}$. For the Hyades, $\sigma_{\rm 3D,obsI} \approx 0.8 \pm 0.15\,{\rm km\,s^{-1}}$, (Röser et al. 2011) and $\sigma_{\rm 3D,obsII} \approx 0.7 \pm 0.07\,{\rm km\,s^{-1}}$ (Oh & Evans 2020). For the Praesepe, the observational results are meagre, but Röser & Schilbach (2019) report $\sigma_{\rm 3D,obs} \approx 0.8\,{\rm km\,s^{-1}}$ (their section 2.3). For both clusters, $\sigma_{\rm 3D,obs}$ is larger by a factor of approximately two than the expected Newtonian value (Table 1). The standard explanation is that this discrepancy is due to additional mass in stellar remnants and a larger measured velocity dispersion due to unresolved multiple stars (cf. Gieles, Sana & Portegies Zwart 2010 for ≈10 Myr old clusters). Open clusters are known to have a deficit of white dwarfs compared to the expected number (Fellhauer et al. 2003) so the contribution by remnants is unclear, and the contribution to the velocity dispersion in proper motion and line-of-sight velocity measurements needs to be assessed with realistic initial binary populations (Dabringhausen et al. 2022). In Milgromian gravitation, the EF-dominated estimate ($\sigma_{\rm M,ef,los}$), on the other hand, is larger than the Newtonian value by only ≈25 per cent, as is confirmed with the PoR simulations in Section 5.1 below. It is unclear, however, how a fully collisional treatment of an open cluster embedded in an external field would enhance the velocity dispersion (see Section 5.4), so that these

[5] The ratio $M_{\rm oc,grav}/M_{\rm oc}$ depends on the EF (Section 3.1).

[6] Analytical estimates of the velocity dispersion of star clusters that have an internal acceleration comparable to the external one ($a_{\rm int} \approx a_{\rm ext} \approx a_0$) are not possible. From equation (9) such clusters would need to have $M_{\rm oc} \approx 10\,000\,{\rm M}_\odot$. Haghi et al. (2019) published interpolation formulae obtained from fits to Milgromian simulations of dwarf galaxies, but these cannot be applied to the star-cluster regime.

estimates have to be taken with great caution. Geometric factors (the density profile) need to be taken into account and the observed values bear some contamination by field stars.

Incidentally, Sollima, Bellazzini & Lee (2012b) analyse the dynamical masses of six globular clusters finding them to be about 40 per cent larger than the stellar-population masses assuming a canonical IMF. The authors include modelling the binary-star population, do not exclude a possible systematic bias, and attribute the larger dynamical masses to retained stellar remnants or the presence of a modest amount of dark matter. For a canonical IMF the remnants, if retained, contribute about 22 per cent of the mass (e.g. fig. 5 in Mahani et al. 2021), although larger fractions are possible as a result of dynamical evolution (see figs 11 and 12 in Baumgardt & Makino 2003; Banerjee & Kroupa 2011). The authors do not discuss Milgromian implications, and it is noted here that the larger effective-Newtonian gravitational masses of the six clusters are qualitatively consistent with the general expectation from Milgromian gravitation. A detailed analysis of the velocity dispersion of the outer halo globular cluster Pal 14 by Sollima et al. (2012a) leads to the cluster being reproducible with Newtonian gravitation. However, Milgromian solutions may be possible if the stellar population lacks low-mass stars. This is possible if Pal 14 formed with an IMF lacking low-mass stars as is expected at low metallicity (Marks et al. 2012; Kroupa et al. 2013; Jeřábková et al. 2018; Yan, Jeřábková & Kroupa 2021). In addition, the initially mass segregated cluster is likely to have lost low-mass stars through early expulsion of residual gas during its formation phase (Marks, Kroupa & Baumgardt 2008; Haghi et al. 2015).

Based on the suggested test for the validity of MOND by Baumgardt, Grebel & Kroupa (2005), the outer halo globular cluster NGC 2419 has been much debated concerning how it fits-in with Milgromian gravitation (Ibata et al. 2011a,b, 2013). According to Ibata et al. (2011a), Ibata et al. (2011b), and Derakhshani (2014) Newtonian models significantly better represent the observed luminosity and line-of-sight velocity dispersion profiles than Milgromian ones, while Sanders (2012) developed Milgromian models that match the observed cluster assuming a strong degree of radial anisotropy. This cluster has a half-mass radius which is about seven times larger than usual globular clusters and is therefore unusual. The phase-space distribution function of stars within the cluster is likely to be affected by the Milgromian phase transition as the cluster orbits from the inner Newtonian Galactic regime into the outer Milgromian regime (Wu & Kroupa 2013). This leads to an anisotropic velocity distribution function of stars in the cluster. Also, violent expulsion of residual gas in Milgromian gravitation when the cluster formed generates a strong anisotropic velocity distribution function (Wu & Kroupa 2018, 2019), and may have changed the mass function of stars in the cluster if it was mass-segregated at birth (cf. Haghi et al. 2015). At birth, the low-metallicity cluster is likely to have been mass-segregated and to have had a top-heavy IMF (Marks et al. 2012; Kroupa et al. 2013; Jeřábková et al. 2018; Yan et al. 2021) through which the innermost regions of the cluster could contain a large fraction of stellar remnants (Mahani et al. 2021) affecting the velocity dispersion profile in the way observed (larger in the innermost region, dropping outwards). More inclusive modelling of this cluster is clearly needed to advance our knowledge of this enigmatic object.

Returning to the tidal tails, as a consequence of the non-linear generalized Poisson equation, the Milgromian potential, Φ, around an open cluster situated within the thin disc of the Galaxy is lopsided. It generates a stronger restoring force towards the cluster on its far side. The external field, $\vec{a}_{\rm ext,kin}$, is directed towards the Galactic centre across the cluster (equation 8). It adds to the radial cluster-centric acceleration on the far side of the cluster relative to the Galactic centre, and it opposes the cluster-centric acceleration field on the near side. Due to the non-linearity of the generalized Poisson equation (equations (4) and (5)), the Milgromian restoring force towards the cluster's centre comes out to be stronger on the far side and weaker on the near side. The cluster's potential is therefore lopsided (Wu et al. 2008; Wu et al. 2010, 2017; Thomas et al. 2018). A visualization of this radial acceleration field is provided by Fig. 3, where the radius, within which the radial acceleration around a point-mass cluster is well approximated by Newtonian gravitation is the MOND radius,

$$r_{\rm M} = \left(\frac{GM_{\rm oc}}{a_0}\right)^{\frac{1}{2}}. \tag{13}$$

While being only a point-mass approximation of the cluster, Fig. 3 thus provides the likely reason why the trailing tail contains fewer stars in the five observed open clusters (Section 2.2). If the cluster generates a constant and isotropic flux of escaping stars through the MOND radius, the higher escape threshold at the far side will deflect a fraction of these back to the cluster such that they are likely to exit on the near side to populate the leading tail.

In order to make a first step towards quantifying the population of escaping stars in the leading versus the trailing tidal tail of an open cluster, the self-consistent code PoR is applied.

4 THE MODELS

Given the non-availability of a Milgromian relaxational (direct n-body) code, a very rough approximation is made to obtain a first insight as to whether Milgromian gravitation might lead to the observed asymmetry in the tidal tails of open star clusters. For this purpose the collision-less (no two-body relaxation) PoR code (Section 3.1) is applied. As a consistency check, Newtonian models of the equivalent Milgromian ones are compared using this same code to test if the former lead to symmetrical tidal tails. Do the Milgromian models develop an unambiguous asymmetry? Is this asymmetry equivalent to the observed asymmetry? And does the asymmetry vary with time?

The underlying energy equipartition process is entirely missing such that the flux of stellar particles across the práh will not be correct: in the simulations, stellar particles leave the cluster by acquiring energy through the time-dependent tidal field as well as through artificial heating due to the limited numerical resolution and not due to two-body encounters. We concentrate on the differential effect (Milgrom versus Newton) and therefore only on the asymmetry, which is governed by the asymmetry of the radial acceleration towards the cluster between the far and near sides (Fig. 3), since the PoR code self-consistently quantifies the shape of the cluster potential.

The computations are performed with the PoR code by applying the 'staticparts patch' (Nagesh et al. 2021), which is available at https://bitbucket.org/SrikanthTN/bonnpor/src/master/. This code allows a subset of dynamical particles to be integrated in time within the background potential of another subset of particles treated as static, i.e. which are not integrated over time. Both Newtonian and Milgromian models have been computed with the exact same numerical procedure. To keep the models as consistent as possible, the selection of the Newtonian model has not been done by switching off the Milgromian option of PoR but by setting the Milgromian constant a_0 to 30 decimal orders of magnitude below the canonical value of $a_0 = 1.2 \times 10^{-10}\,{\rm m\,s^{-2}} \approx 3.8\,{\rm pc\,Myr^{-2}}$.

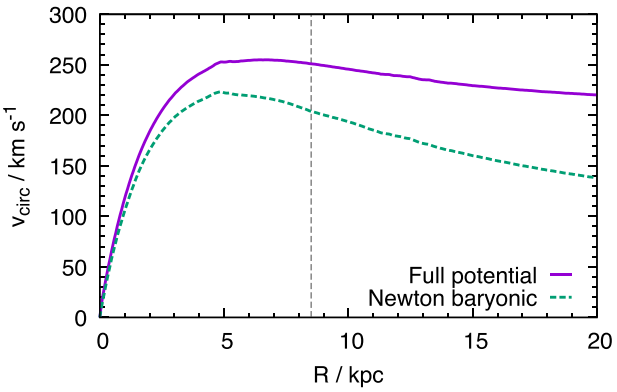

Figure 4. The rotation curves for the total gravitational potential (Milgrom or Newton plus DM halo, solid purple line) and the Newtonian baryonic component (dashed green line). The vertical dashed line marks the orbital distance of the model clusters from the Galactic centre.

In the following, the Galactic potential used (Section 4.1) and the cluster models (Section 4.2) are described.

4.1 The galactic potential

For a comparison of equivalent Newtonian versus Milgromian models, it is necessary to insert the same cluster model on the same initial orbit into a galaxy which has the same rotation curve at the position of the cluster. Thus, the tidal effects in the two galaxy models are comparable, one being purely baryonic in Milgromian dynamics, the other being Newtonian with the same baryonic component and with an additional spherical dark matter (DM) component. To achieve a rotation curve which matches that observed for the Galaxy nearby to the Sun, the baryonic component is modelled as two radial exponential and vertical sech^2 discs: Component I has an exponential scale-length of 7 kpc and an exponential scale height of 0.322 kpc making up 17.64 per cent of the total baryonic mass. Component II has a scale-length of 2.15 kpc and a scale height of 0.322 kpc making up 82.64 per cent of the total baryonic mass. We emphasize that this is not meant to be an exact representation of the Galaxy but merely a description sufficiently realistic to provide a radial and perpendicular approximation of the Galactic accelerations near the Solar circle. The density distribution of the DM component is defined to match the Milgromian rotation curve shown in Fig. 4. Thus the Galaxy is automatically on the radial-acceleration relation (RAR, McGaugh, Lelli & Schombert 2016; Lelli et al. 2017) and on the baryonic Tully–Fisher relation (BTFR, McGaugh et al. 2000; McGaugh 2005; Lelli, McGaugh & Schombert 2016) in both cases. The DM halo is truncated outside 10 kpc to save computing ressources. This is physically justified since the cluster models orbit the Galactic centre at $R_{gal} \approx 8.3$ kpc, i.e. well within the truncation radius. In Newtonian gravity, the field of a spherically symmetrical shell cancels out inside the shell, so any DM component outside the orbit of any cluster particle can be ignored. This is, however, not true for the non-spherical disc potential, therefore a disc template with a maximum radius of about 50 kpc is employed. Since both galaxy models only serve as a constant background potential, no velocity component needs to be added, but rather the galaxy + DM particles are treated as static gravity sources.

The models invoke 30 million static particles to provide a smooth background potential. In the Newtonian DM case another 10 million static particles are used for the DM halo.[7] The minimum and maximum grid refinement levels are set to 7 and 21, respectively. In the computations, however, the maximum refinement level actually reached is only 17. Given a total box length of 256 kpc, this corresponds to a spatial resolution of about 1.95 pc. The dynamical subset consists of the stellar particles of the model clusters introduced in the next section.

4.2 Milgromian and Newtonian models of open clusters

In the Solar neighbourhood, open clusters are well described by a Plummer phase-space distribution function (Röser et al. 2011; Röser & Schilbach 2019), which corresponds to a King model with a concentration parameter $W_o \approx 6$ (Kroupa 2008).[8] The spherical and isotropic PoR cluster models are therefore set up as Plummer phase-space distribution functions.

The Newtonian Plummer models are initialized following Aarseth et al. (1974). The Milgromian Plummer models are constructed as follows. First, a Newtonian Plummer model is set-up using the Newtonian method. A Milgromian velocity scaling factor f_M is introduced as

$$f_M = \sqrt{\nu(y)}, \tag{14}$$

with $\nu(y) = \sqrt{1/4 + 1/y} + 1/2$, $y = g_N/a_0$, being the Milgromian–Newtonian transition function, and $g_N = |\vec{a}_N|$ with $\vec{a}_N = \vec{a}_{i,N} + \vec{a}_{ef,N}$ is the Newtonian acceleration obtained by adding the internal and external Newtonian accelerations. The particle velocities $\vec{v}_{i,M}$ are then derived from the Newtonian model velocities, $\vec{v}_{i,N}$, via

$$\vec{v}_{i,M} = f_M\, \vec{v}_{i,N}. \tag{15}$$

The Newtonian internal acceleration $\vec{a}_{i,N}$ is taken directly from the Newtonian Plummer model, while the Newtonian external field component, $\vec{a}_{ef,N}$, is related to the actual Galactic external field, $\vec{a}_{ext,kin}$, via

$$\vec{a}_{ef,N} = \mu(x)\, \vec{a}_{ext,kin} \tag{16}$$

with

$$\mu = x/(x+1), \quad x = a_{ext,kin}/a_0 \tag{17}$$

(section 4.2.2. in Lüghausen et al. 2015), being the inverse transition function and $a_{ext,kin} = |\vec{a}_{ext,kin}| = v_{circ}^2/R_{gal}$ in the direction to the Galactic centre. Since $a_{ext,kin} \approx 7.5\,\mathrm{km\,s^{-2}}$ (Table 1), $\mu \approx 0.66$ in the present context.

The real open clusters (Table 1) have masses of a few hundred $M_\odot$ and half-mass radii ($r_h \approx 1.3 \times r_{pl}$) near 4 pc, which is a regime that the particle-mesh models cannot resolve adequately because the density contrast to the surrounding field is too small and available computational resources constrain the reachable refinement level.

[7]The rotation curve (Fig. 4) is higher by about 10 per cent than in the real Galaxy that has $v_{circ} \approx 220\,\mathrm{km\,s^{-1}}$ because the initialization through a particle dark matter halo (for the Newtonian models) has this amount of uncertainty. We leave the models at the slightly higher v_{circ} and adopt this higher value also for the Milgromian models as the model clusters need to be computed in a comparable tidal field.

[8]That the well-observed open and globular clusters, which are the simplest (coeval and equal-metallicity) stellar populations, are next-to-perfectly described by the Plummer phase-space distribution function (Aarseth, Henon & Wielen 1974; Plummer 1911; Heggie & Hut 2003), which is the simplest analytical solution of the collision-less Boltzmann equation, is interesting and deserves emphasis. Note that the Milgromian models retain a Plummer density distribution as they evolve (Fig. 5 below).

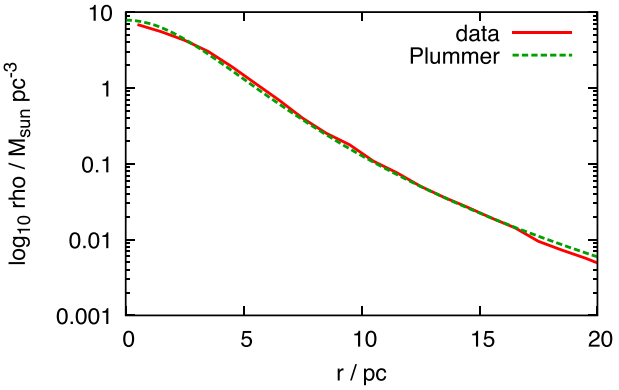

Figure 5. The volume density Plummer fit (green dashed line) versus the density for the $M_{\rm oc,0} = 5000 M_\odot$ Milgromian cluster (solid red line, model cM3) at 500 Myr. Note that the simulated model is next-to-perfectly represented by the Plummer model with Plummer radius $r_{\rm npl} = 4.9$ pc.

The approach taken here is to start with a large $M_{\rm oc,0} = 2 \times 10^4 M_\odot$ and to initialize a set of cluster models with decreasing mass but with the same theoretical Plummer radius, $r_{\rm pl} = 10$ pc ($r_{\rm h} \approx 13$ pc). While the initial Plummer model is set-up with this Plummer radius, a numerical alteration to the particle distribution is needed to avoid strong mass loss at the beginning: A numerical model inserted within the disc of the galaxy does not correspond to the analytical Plummer phase space distribution function, which is bounded in mass but unbounded in radial extend. Particles that are at too large cluster-centric distances are unbound in the numerical model. Particles outside $r = r_{\rm pl}$ are therefore re-positioned to be inside $r_{\rm pl}$ and the kinetic energy is reset to a value corresponding to a particle orbiting inside $r_{\rm pl}$. This stabilizes the cluster against initial mass loss, however, it also effectively compactifies the cluster. After a brief period of settling, the cluster models stabilize at an effective Plummer radius of about $r_{\rm npl} \approx 4.5$ pc initially. The models remain excellent approximations to the Plummer model (Fig. 5 below) and the Plummer radius increases with time as the cluster loses mass and thus becomes less bound.

The models are created to have a velocity dispersion that reaches that of the Hyades cluster in order to achieve a comparable dynamical state. The full computed set comprises Milgromian and Newtonian models with $M_{\rm oc,0} = 2500, 3500, 5000, 6000, 7000, 8500, 10\,000, 12\,000, 14\,000, 20\,000 M_\odot$. Each model is composed of $0.1 M_\odot$ equal mass particles such that the Plummer phase-space distribution function is well sampled and different initial random number seeds do not affect the results. The models are computed over 1 Gyr. Only five in each set (with $M_{\rm oc,0} = 2\,500$, $3\,500$, 5000, 7000, $10\,000 M_\odot$) are analysed in more detail, the heavy models being not representative of the observed open clusters by having too large velocity dispersions (Fig. 10 below). The initial analytical Plummer 3D velocity dispersion in Newtonian gravitation (Heggie & Hut 2003; Kroupa 2008),

$$\sigma_{\rm ch} = \left(\frac{3\pi}{32} \frac{G\, M_{\rm oc,0}}{r_{\rm Pl}} \right)^{\frac{1}{2}}, \tag{18}$$

is, for the full set of models, in the range $\approx$0.86–2.43 km s^{-1} for $r_{\rm pl} = r_{\rm npl} \approx 4.5$ pc, being near the range of the real open clusters (Table 1, see Fig. 10 below for the velocity dispersions at 500 Myr). Since the effective-Newtonian gravitational mass of an open cluster in the Solar neighbourhood is $M_{\rm oc,grav} \approx 1.5\, M_{\rm oc}$, it follows that the Milgromian 3D velocity dispersion of the models should be

$$\sigma_{\rm ch,Mil} \approx 1.2\, \sigma_{\rm ch}. \tag{19}$$

The tidal radius of a cluster can be approximated as

$$r_{\rm tid} \approx \left(\frac{M_{\rm oc}}{K\, M_{\rm MW,grav}} \right)^{1/3} R, \tag{20}$$

where $K = 2$ for the logarithmic ($K = 3$ for a point-mass) galactic potential, and $M_{\rm MW,grav} = (R/G)\, v_{\rm circ}^2$ ($M_{\rm MW,grav} \approx 1.15 \times 10^{11} M_\odot$ within $R = 8300$ pc for the MW with $v_{\rm circ} = 250$ pc Myr^{-1}). Since the initial tidal radii of the models are in the range $18 \lesssim r_{\rm tid,0}/{\rm pc} \lesssim 37$, the shape of the zero-potential surface which defines the cluster práh is well resolved such that the anisotropy of the flux of escaping particles should adequately approximate the true anisotropy allowing a physically correct comparison of the Newtonian (symmetrical surface, anisotropy expected to be negligible) with the Milgromian (non-symmetrical surface, Fig. 3) models.

The real clusters (Table 1) are currently on orbits that are nearly circular with $0.03 < e < 0.12$. The inclination angles, ι, relative to the Galactic mid-plane are also small ($\tan(\iota) = z_{\rm max}/R$, $\iota < 1^\circ$). Given the explorative nature of this work, the models are initialized on circular orbits within the mid-plane of the galactic model. Future work will address more realistic, slightly inclined orbits. The current orbits end up being slightly eccentric in the actual discretized galaxy potential. In order to track the orbit of the cluster, the density centre of each model cluster is calculated using the density measurement method described by Casertano & Hut (1985) and the density centre position formula by von Hoerner (1963). Given an ensemble of n stellar particles, the local density around any stellar particle i of mass $m_{\rm i}$ is defined in the volume of the distance to its jth neighbour,

$${}^j\rho_{\rm i} = \frac{j-1}{V(r_{{\rm i},j})}\, m_{\rm i}, \tag{21}$$

where $r_{{\rm i},j}$ is the distance from stellar particle i to its jth neighbour and $V(r_{{\rm i},j}) = 4\pi\, r_{{\rm i},j}^3/3$ is the volume of the enveloping sphere. The galactocentric position of the density centre is then defined as the density-weighted average of the positions of the stellar particles,

$${}^j\vec{R} = \frac{\sum_{\rm i=1}^{n_{\rm tid}} \vec{R}_{\rm i}\, {}^j\rho_{\rm i}}{\sum_{\rm i=1}^{n_{\rm tid}} {}^j\rho_{\rm i}}, \tag{22}$$

where $n_{\rm tid}$ is the number of stellar particles within the initial tidal radius, $r_{\rm tid,0}$ (as a simplification this radius cut-off is kept constant), and $\vec{R}_{\rm i}$ is the galactocentric position vector of particle i. Following the suggestion by Casertano & Hut (1985), $j = 6$ is used in this study. It emanates that the orbits are not perfectly smooth (Fig. 13) as a consequence of the live dynamical computation of the cluster centre. For the calculation of the cluster specific angular momentum, its velocity dispersion and the asymmetry of the tidal tails, the position of the density maximum is used as the reference.

5 RESULTS

5.1 The cluster profile, evolution of model mass, and velocity dispersion

As noted in Section 4.2, the observed density profiles of open clusters are well fit by the Plummer profile. The present models are initialized as Plummer phase-space density distribution functions, but do they retain Plummer profiles as they evolve? The numerical density profile of the Milgromian $5000 M_\odot$ cluster at an age of 500 Myr is shown in Fig. 5. The numerical model is well represented by an analyitcal Plummer density distribution, as is the case for all the other models.

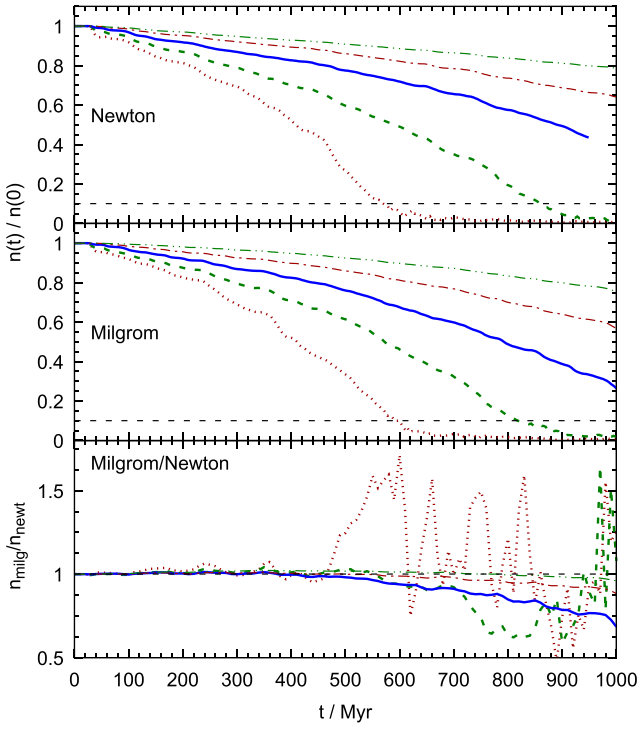

Figure 6. The relative number of stellar particles within the initial tidal radius (equation 20) as a function of time in the five models with an initial mass of $M_{\rm oc,0} = 2500$, 3500, 5000 (blue), 7000, and 10 000 $M_\odot$ (bottom to top). Top panel: Newtonian models, middle panel: Milgromian models, bottom panel: ratio of the two. Note that the Milgromian models dissolve faster than the Newtonian models. The fluctuations in the ratio (bottom panel) is large for the least-massive models (red dotted lines) due to the small number of particles and the PoR code not well-resolving their weak potentials. The general trend is for the less-massive Milgromian models to dissolve faster than the more massive ones, and, at a given mass for them to dissolve faster than their Newtonian counterparts. The horizontal dashed lines in the upper two panels correspond to the 10 per cent dissolution threshold.

The models dissolve by loosing stellar particles as is shown in Fig. 6. As for real star clusters, the low-mass models dissolve more rapidly than the more massive ones. Compared to realistic Newtonian calculations using the direct n-body method, which have $n(t)$ decrease following a concave curve (i.e. with a slight slow-down of the evaporative stellar loss with decreasing $n(t)$, e.g. fig. 1 in Baumgardt & Makino 2003), the present models show an increasing rate of loss of stellar particles with time. This occurs because the adaptive-mesh method reduces the refinement with decreasing density that compromizes the accuracy of tracing the forces, leading to an artificial speed-up of mass loss. This is not a problem for the purpose of the present study which is concerned with the asymmetry of the tidal tails which probes the asymmetry of the potential generated by the cluster–Galaxy pair, but implies that the lifetimes of the present models cannot be applied to real open clusters, although they allow an assessment of the relative lifetimes between the Milgromian and Newtonian cases. Beside the effect of the adaptive mesh, the different shape of the mass evolution obtained here (convex) compared to collisional n-body simulations (concave) is due to two-body relaxation in the collisional n-body simulations leading to cluster core contraction as energy-equipartition-driven mass loss occurs, thus increasing the binding energy of the cluster and its resistance to tidal effects (e.g. Baumgardt & Makino 2003).

The more rapid dissolution of the Milgromian models compared to the Newtonian ones (Fig. 6) can be understood as follows: Given a small loss of mass, $\delta M_{\rm oc}$, the change in binding energy of a Newtonian star cluster is $\delta E_{\rm bind,N} \approx (2/r_{\rm grav})\, G\, M_{\rm oc}\, \delta M_{\rm oc}$, where $r_{\rm grav}$ is the gravitational radius of the cluster. The here-relevant open clusters (Table 1) are near-Newtonian but with a larger effective gravitational constant, $G_{\rm eff} \approx 1.5\, G$ (equation 12). Thus, for the same mass loss of $\delta M_{\rm oc}$, a Milgromian open cluster of the same mass and radius suffers a reduction of its binding energy relative to that of the Newtonian case, $\delta E_{\rm bin,M}/\delta E_{\rm bind,N} \approx G_{\rm eff}/G \approx 1.5$. The Milgromian models can be understood to dissolve more rapidly as a consequence of more rapidly loosing their binding energy (see also Section 5.5).

The Milgromian open clusters are expected to be super-virial when compared to their Newtonian counterparts (Table 1). Thus, it is of interest to consider how super-virial the here-computed Milgromian cluster will appear to a Newtonian observer. For the purpose of comparing the velocity dispersion of the Newtonian and Milgromian models at the same stage of dissolution, it is useful to estimate their dissolution time. Because the more massive models are not computed to complete dissolution, the lifetimes of the Newtonian model clusters are estimated as follows: First, the decay times of the two least massive models (2500 and 3500$M_\odot$) down to 1/10th of the initial mass are extracted from the data. These are defined as their lifetimes, $t_{\rm life,N}$, being 570 and 854 Myr, respectively.[9] Given the mass ratio of 0.714, this corresponds to an exponent of about 1.2, $t_{\rm life,N}/{\rm Myr} \approx 570\,(M_{\rm oc,0}/(2500{\rm M}_\odot))^{1.2}$. The resulting approximate lifetimes are then $t_{\rm life,N} \approx 570$ Myr for 2500$M_\odot$, 860 Myr for 3500$M_\odot$, 1300 Myr for 5000$M_\odot$, 2000 Myr for 7000$M_\odot$, and 3000Myr for 10 000$M_\odot$. For the Milgromian models we obtain likewise $t_{\rm life,M}/{\rm Myr} \approx 595\,(M_{\rm oc,0}/(2500{\rm M}_\odot))^{0.95}$. Note that the Milgromian model with the initial mass $M_{\rm oc} = 2500{\rm M}_\odot$ dissolves slightly later (at 595 Myr) than the Newtonian model of the same initial mass (570 Myr). Studying Fig. 6, one can see that the red dotted curve has significant fluctuations such that this difference is not significant. The here estimated PoR lifetimes merely serve to define the time-scale over which the velocity dispersion is calculated, and also as an indication of the ratio, $t_{\rm life,M}/t_{\rm life,N}$, as a consequence of loss of particles across the práh through non-relaxational processes (probably mostly orbital precession, as discussed in Section 5.4). The elapsed relative time is then divided by the lifetime for each cluster model. For the least massive cluster, the existing simulation data correspond to as much as 1.8 lifetimes since the simulation ran for 1000 Myr and thus continued some 430 Myr after the effective decay of that model. This allows the tidal tails to be traced because the stellar particles continue to orbit the Galaxy after the dissolution of the cluster model.

The 3D velocity dispersion in a model is

$$\sigma_{\rm 3D} = \left(\frac{1}{n_{\rm tid}} \left(\sum_{\rm i=1}^{n_{\rm tid}} \vec{v}_{\rm i}^{\,2} \right) \right)^{\frac{1}{2}}, \qquad (23)$$

where $\vec{v}_{\rm i}$ is the velocity vector of particle i relative to the model cluster's centre.

In Fig. 7, the ratio of $\sigma_{\rm 3D}$ for the Milgromian and Newtonian models is shown as a function of time. The Milgromian models consistently have a velocity dispersion which is about 20 per cent larger than the Newtonian models with excursions to ratios as large as 1.4. The tendency is that the less-massive models show a larger ratio, but

[9]Note that an open cluster with $M_{\rm oc} = 2500{\rm M}_\odot$ would, in Newtonian gravitation, dissolve in $T_{\rm diss} \approx 3$ Gyr, equation (1).

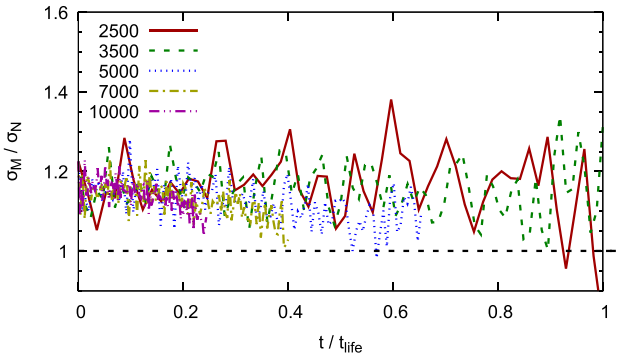

Figure 7. The ratio of the Milgromian to Newtonian 3D velocity dispersion (equation 23) as a function of relative time for the five cluster models (the initial masses in $M_\odot$ of which are indicated in the legend). The relative time is $t/t_{\rm life} = 1$ when the model has lost 90 per cent of its stellar particles. The data are truncated to the lifetime to focus on the most meaningful data range.

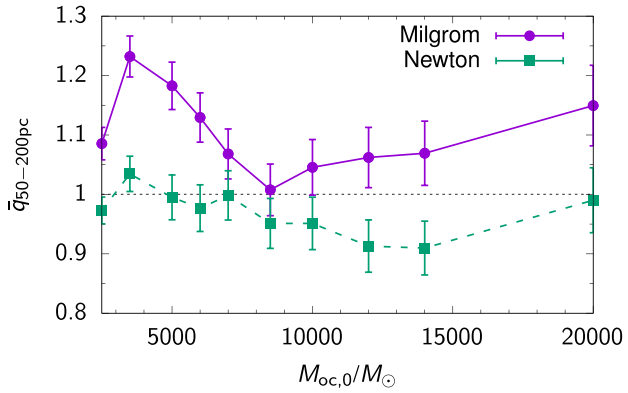

Figure 9. The number ratio between the leading and trailing tidal arm in the cluster-centric distance range 50–200 pc and averaged over 400–800 Myr as a function of the initial model cluster mass $M_{\rm oc,0}$. The green dashed line corresponds to the Newtonian models while the purple solid line shows the results for the Milgromian models. The errorbars indicate the 5-σ Poisson errors. The dependence of the ratio on the velocity dispersion is shown in Fig. 11.

given the limitation of the numerical method applied, it is not possible to assess this ratio for a model with a mass as low as the observed open clusters in Table 1. The analytically calculated Milgromian velocity dispersion documented in this table under the influence of the EF provides a similar estimate (compare $\sigma_{\rm M,ef,los}$ with $\sigma_{\rm N,los}$).

Concerning the overall structure of the model tidal tails, snapshots of the simulation with $M_{\rm oc,0} = 5000 M_\odot$ in Newtonian and Milgromian dynamics are shown in Fig. 8 as an overview (left-hand panels) and zoomed-in (right-hand panels). Note the apparent asymmetry in the number of particles: the leading (rightwards) tidal tail has more particles (see the bottom left-hand panel) relative to the number in the trailing tail in the Milgromian model compared to the Newtonian one that appears much more symmetrical as should be the case in Newtonian gravitation (Fig. 9). This asymmetry is consistent with the basic consequence of Milgromian gravitation, namely that the far-side (to the left) of the cluster has a larger barrier against escape than the near side, as evident in Fig. 3.

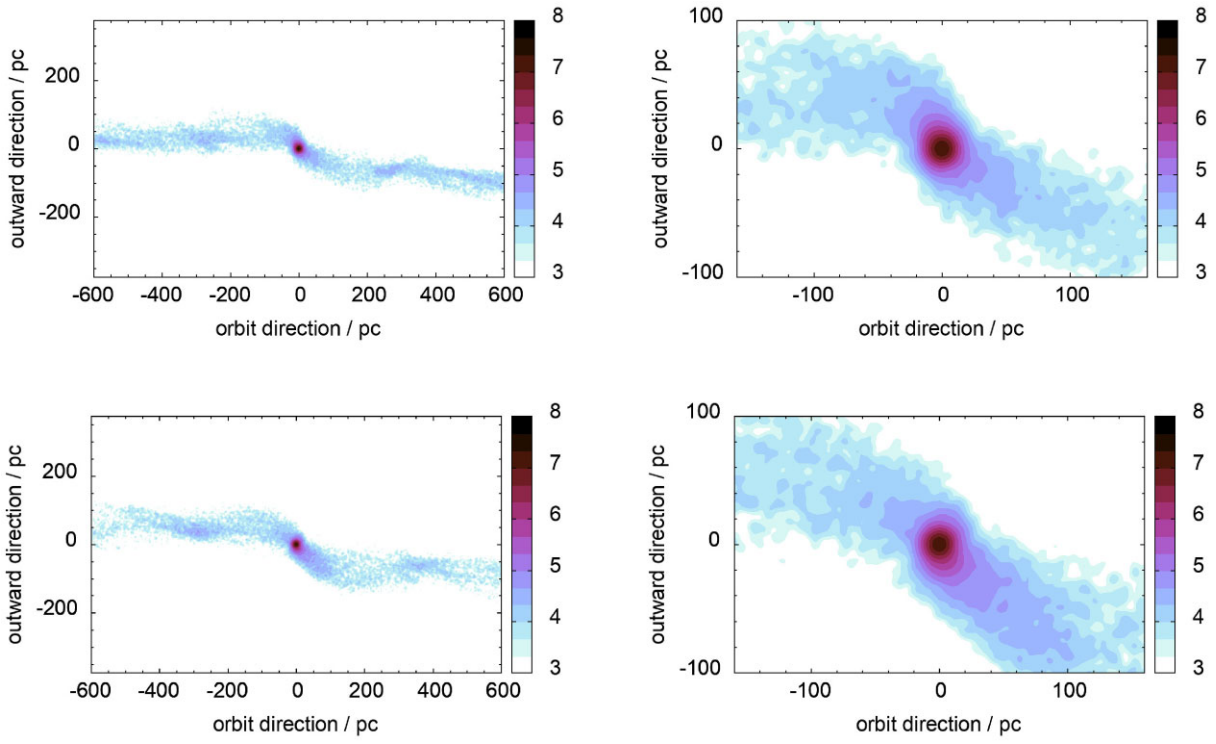

Figure 8. Snapshot of the cluster model with initial mass $M_{\rm oc,0} = 5000 M_\odot$ at 600 Myr in Newtonian (upper two panels) and Milgromian (lower two panels) dynamics. The right-hand panels are detailed views of the model's surroundings. Note the lopsided shape of the Milgromian model, which is consistent with previous work (Wu et al. 2008; Wu et al. 2010, 2017; Thomas et al. 2018). The galactic centre is towards the bottom of the plot and the orbital direction is to the right. The surface density scale (key to the right of each panel) is in $\log_{10}(M_\odot\,{\rm kpc}^{-2})$ and is for illustration only. The colour scale has been divided into discrete steps to enhance the visibility.

The visual appearance of the tail asymmetry near to the Milgromian model clusters in Fig. 8 resembles the previously published images of the tidal tails close to the Hyades, Coma Berenices, Praesepe and COIN-*Gaia* 13 clusters (Section 2.2).

In Newtonian dynamics, the first Küpper overdensities are equidistant from the open cluster in the leading and trailing tail and move to a smaller distance from the open cluster as the cluster evaporates (Küpper et al. 2008, 2010; Küpper et al. 2012). The two distances between the centre of the cluster and the two first overdensities can be used to measure the effective-Newtonian gravitational mass of the cluster (Küpper et al. 2015). We refrain from doing so here since the computed models are exploratory and we do not want to over-interpret them. The models are useful for probing the asymmetry between the two distances, as this may be an additional diagnostic for assessing whether Newtonian or Milgromian gravitation is closer to reality. Due to the cluster-centric potential being asymmetrical in Milgromian gravitation (Fig. 3), the distances between the overdensities are expected to differ. Indeed, in this simulation, the first Küpper epicyclic overdensity is located at ±270 pc in the Newtonian models (Fig. 8), while the Milgromian models have the leading overdensity located at +360 pc and the trailing one at −290 pc. The larger cluster-centric distance in the leading tail comes from the particles spilling across the práh into the leading tail having larger velocities due to the smaller potential barrier at the first Lagrange point. That both Küpper overdensities are at larger distances from the cluster centre in Milgromian dynamics than in Newtonian dynamics is due to the larger effective-Newtonian gravitational mass of the former. This Milgromian asymmetry and Newtonian symmetry appears to be evident in the observed and modelled tidal tails of the globular cluster Pal 5, respectively (figs 7 and 8 in Erkal et al. 2017: the observed leading Küpper overdensity being at coordinate $\phi_1 = -0.7$ and the trailing one being at $\phi_2 = +0.6$ with the cluster at $\phi = 0$), but its non-circular orbit complicates the interpretation and no conclusive conclusion can emanate. Noteworthy in this context is that modelling a satellite galaxy in Newtonian gravitation, Reinoso, Fellhauer & Véjar (2018) find the position of the first Küpper overdensity to be correlated with the orbital distance and the mass of the satellite. They also find the first Küpper epicyclic overdensity to be closer to the satellite in the leading tail than in the trailing tail (their fig. 5). The authors argue that this asymmetry, which is inverted to the asymmetry of the present Milgromian star-cluster models, 'could be explained by the fact that we have a much more extended object than used in the previous study.' A follow-up study will address this aspect (the relative distances of the Küpper overdensities in the leading and trailing tails) to probe how these can be employed as a test of gravitational theory.

5.2 Time-averaged leading-to-trailing tail number ratio, $\overline{q}_{50-200\,\mathrm{pc}}$, in terms of model mass and velocity dispersion

As a next step in the analysis, the ratio of the number of particles in the leading versus the trailing tail per output time, $q(t)$, is computed for the Newtonian and Milgromian models. To calculate $q(t)$, it is necessary to distinguish between particles from each tail. The coordinate system is first translated to the position of the density centre of the model cluster. The coordinates refer to the galactic coordinate system, i.e. the X-axis points towards the galactic centre and Y is along the orbital motion. A dividing line is defined through the density centre at an angle of 45° (counterclockwise), therewith lying at about a right angle relative to the inner tidal tails (i.e. a diagonal from the lower left to the upper right passing through the position of the cluster centre in Fig. 8). The number of particles to the left and right of this line enumerates, respectively, the numbers in the trailing and the leading arms. As for the real clusters (Section 2.2), $q_{50-200\,\mathrm{pc}}(t)$ is calculated between model cluster-centric radial limits of $d_{\mathrm{cl}} = 50$ and 200 pc (but see Fig. 12 for an exploration of different ranges). Since the tails consist of particles that drift away from the models, $q_{50-200\,\mathrm{pc}}(t)$ is here time-averaged between 400 and 800 Myr, covering the ages of the observed clusters in Table 1, yielding $\overline{q}_{50-200\,\mathrm{pc}}$.

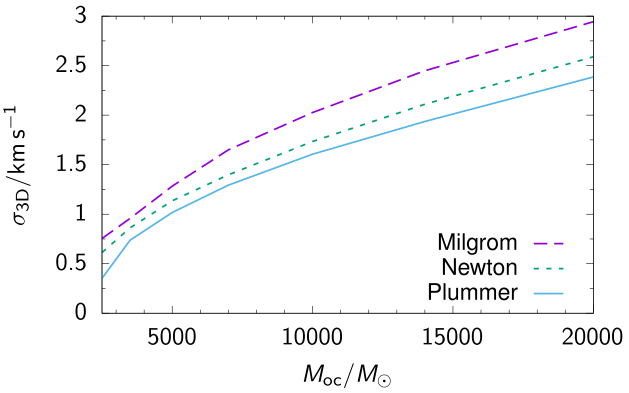

Figure 10. The numerically calculated 3D velocity dispersion, $\sigma_{3D,}$ of all particles within the initial $r_{\mathrm{tid}}(0)$ of the cluster centre is shown at 500 Myr for the Newtonian (short-dashed blue) and Milgromian (long-dashed purple) models. The analytical Newtonian characteristic velocity dispersion, σ_{ch} (equation 18), is plotted as the solid blue line.

Fig. 9 shows $\overline{q}_{50-200\,\mathrm{pc}}$ in dependence of the model cluster mass. The Newtonian models have $0.85 < \overline{q}_{50-200\,\mathrm{pc}} < 1.03$, being close to unity for the smaller model masses but showing an increasing departure towards $\overline{q}_{50-200\,\mathrm{pc}} < 1$ for the more massive models except for the most massive model. The Milgromian models, on the other hand, have $1.01 < \overline{q}_{50-200\,\mathrm{pc}} < 1.25$. Note the apparent systematic variation of the Milgromian $\overline{q}_{50-200\,\mathrm{pc}}$ from $\overline{q}_{50-200\,\mathrm{pc}} \approx 1.25$ for $M_{\mathrm{oc},0} = 3500\mathrm{M}_\odot$ to a minumum near $M_{\mathrm{oc},0} = 8500\mathrm{M}_\odot$ with an increase again towards larger masses (the value of $\overline{q}_{50-200\,\mathrm{pc}}$ for $M_{\mathrm{oc},0} = 2500\mathrm{M}_\odot$ may be affected by the limited resolution). For the time being it remains unclear if this systematic behaviour of $\overline{q}_{50-200\,\mathrm{pc}}$ is a real feature.

Given the time-averaged systematic change of $\overline{q}_{50-200\,\mathrm{pc}}$ with $M_{\mathrm{oc},0}$, this behaviour is next probed in terms of the 3D velocity dispersion, σ_{3D}, of the cluster models. This might lead to insights concerning the real open clusters since the models are, by numerical necessity, much more massive than the real clusters. By having larger radii, the velocity dispersion falls into the range of the observed open clusters ($\approx$0.8 km s^{-1}).

For all cluster models in both Newtonian and Milgromian dynamics, a Plummer sphere is fitted through the volume density distribution out to a radius of 20 pc. The free parameters are the Plummer radius, r_{Pl}, and the cluster mass, M_{oc} (e.g. Fig. 5). The velocity dispersion, σ_{3D}, is calculated within the initial tidal radius at 500 Myr. The time of 500 Myr ensures the clusters to be well virialized while the lowest-mass models are still not too dissolved. The velocity dispersions of the models is shown in Fig. 10. As can be seen from the diagram, the velocity dispersion in the numerical Milgromian case is about 20 per cent higher than in the numerical Newtonian case and about 25 per cent higher than in the corresponding analytical Plummer Newtonian models. This is also evident in Fig. 7.

Fig. 11 shows $\overline{q}_{50-200\,\mathrm{pc}}$ for the Newtonian and Milgromian cases as a function of the respective velocity dispersion. Both, the Newtonian

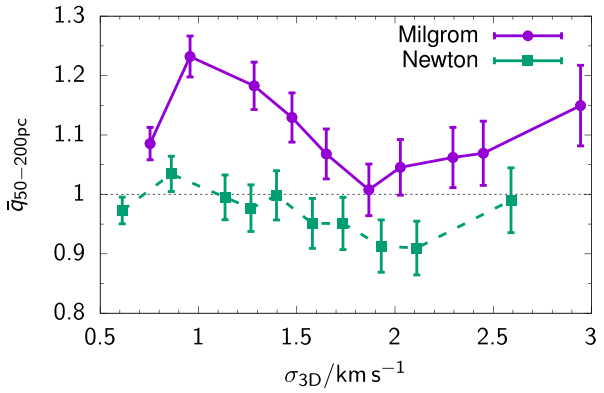

Figure 11. Same as Fig. 9 (the models are the same from left to right), but showing $\overline{q}_{50-200\,\mathrm{pc}}$ as a function of the velocity dispersion (Fig. 10) of the models at 500 Myr. Note the same shape of the dependency as in Fig. 9 and that at the same mass, the Milgromian models have a larger velocity dispersion. The observed Hyades and Praesepe have an observed 3D velocity dispersion near 0.8 $\mathrm{km\,s^{-1}}$ (Section 3.2.2), which, according to these results, is near to where the systems achieve the maximum tail asymmetry in the Milgromian models.

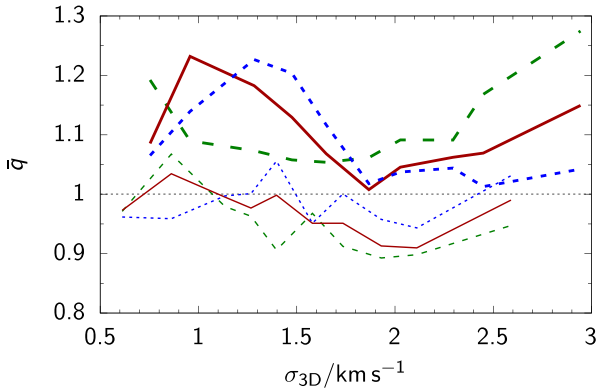

Figure 12. Same as Fig. 11, but for different radial averaging intervals. Milgromian (Newtonian) models are shown as thick (thin) lines. The solid line corresponds to the 50–200 pc interval, the dashed line to the 50–100 pc interval, and the dotted line to the 50–300 pc interval. The errorbars are omitted for better visibility and because the errors are similar for all averaging intervals.

and Milgromian models show a comparable shape of the $\overline{q}_{50-200\,\mathrm{pc}}$ versus σ_{3D} numerical data with a minimum near $\sigma_{3D} \approx 2\,\mathrm{km\,s^{-1}}$, but the Milgromian models are systematically asymmetrical with the leading tail containing significantly more stellar particles than the trailing tail in the distance range 50 to 200 pc from the cluster centre. Fig. 12 displays also the additional intervals 50–100 pc and 50–300 pc, demonstrating that the $\overline{q}_{50-200\,\mathrm{pc}} > 1.1$ asymmetry remains comparable in the Milgromian models, while the Newtonian models have values of $\overline{q}_{50-200\,\mathrm{pc}}$ closer to 1 in all cases.

5.3 $q_{50-200\,\mathrm{pc}}$ as a function of time: models versus observations

How do these results compare with observations?

A direct comparison between the model- and real-cluster- $q_{50-200\,\mathrm{pc}}$ values needs to be made with due caution because it is not clear if the values actually depend on the mass or the velocity dispersion of the clusters, and because the models suggest the Milgromian prediction of $q_{50-200\,\mathrm{pc}}$ to vary with the Galactocentric orbital phase (as discussed below) with this information not being available for the real clusters. But the comparison with the observations is valuable because it shows that the observed tidal tail asymmetry is not expected in Newtonian dynamics while it can occur in the Milgromian framework. The asymmetry ratio, $q_{50-200\,\mathrm{pc}}$, of the real clusters (Table 1) cannot be plotted versus the theoretical initial mass, $M_{\mathrm{oc},0}$ (to be equivalent to Fig. 9 for the models), because the present-day masses of the real clusters are highly uncertain. These have not been well constrained, propagating through to a significant uncertainty in their initial masses, $M_{\mathrm{oc},0}$. The ages of the real clusters are better constrained though, and Fig. 13 plots $q_{50-200\,\mathrm{pc}}$ versus age for these.

The Hyades (square) has $q_{50-200\,\mathrm{pc}} = 2.53 \pm 0.37$ and for NGC 752 (upside down open triangle) $q_{50-130\,\mathrm{pc}} = 1.30 \pm 0.24$, Coma Berenices (circle) has $q_{50-200\,\mathrm{pc}} = 1.2 \pm 0.15$ and the Praesepe (triangle) has $q_{50-200\,\mathrm{pc}} = 0.62 \pm 0.08$. The latter case appears to contradict the expectation from the above theoretical analysis that $q_{50-200\,\mathrm{pc}} > 1$ always if Milgromian gravitation were to be correct. Note that this apparent contradiction would not salvage Newtonian gravitation because of the simultaneous (now on-going) similar asymmetry of the Hyades, Coma Berenices and NGC 752 tails. A clue to this problem is obtained by noting that the data may suggest an age sequence of $q_{50-200\,\mathrm{pc}}$.

This is tested for in Fig. 13 by plotting the temporal evolution of $q_{50-200\,\mathrm{pc}}(t)$ for five models with $\sigma_{3D} < 2\,\mathrm{km\,s^{-1}}$ constituting computationally-reachable approximate conformity with the observed open clusters. For $t \lesssim 100$ Myr, the models are evolving into an equilibrium mass-loss rate across the $d_{\mathrm{cl}} = 50$ pc to 200 pc distance range. After ≈400 Myr, the Newtonian models are limited to $0.6 < q_{50-200\,\mathrm{pc}}(t) < 1.4$, while the Milgromian models have $q_{50-200\,\mathrm{pc}}(t)$ oscillating near-periodically between 0.6 and 2.5. The present computations indicate the clusters to show an encouraging agreement with the Milgromian models within the $1\,\sigma$ error ellipse since these rise to the level of the observed asymmetry (Fig. 13). Noteworthy is that the Milgromian models show oscillations in $q_{50-200\,\mathrm{pc}}(t)$ with it increasing to larger values when the models are near perigalacicon to afterwards fall slightly below $q_{50-200\,\mathrm{pc}} = 1$.

As a caveat and reminder though: while consistency with the Milgromian models is evident, the Newtonian PoR models are inconsistent at more than 5 sigma confidence only with the Hyades datum with the other three clusters being also consistent with the Newtonian PoR models. Before reaching final conclusions on which theory of gravitation is valid, more observational work is needed to improve the quantification of the tidal tail asymmetry.

5.4 Why does $q_{50-200\,\mathrm{pc}}(t)$ oscillate?

With the aim to shed some light on the question why the Milgromian models have an oscillating $q_{50-200\,\mathrm{pc}}(t)$ with maxima occurring near the cluster's peri-galactica, the velocity dispersion and spin angular momentum of the cluster models are studied next. The notion is that groups of stellar particles might be moving in a correlated manner within the cluster to exit across the práh together as the Milgromian cluster potential adjusts, causing the momentary flare-like increase of $q_{50-200\,\mathrm{pc}}(t)$.

The bulk 3D velocity dispersion of the stellar particles within the tidal radius, $\sigma_{3D}(t)$ (equation 23), is plotted in Fig. 14. Neither the Milgromian nor the Newtonian models show a near-periodic change in $\sigma_{3D}(t)$ that resembles the quasi-periodic evolution of $q_{50-200\,\mathrm{pc}}(t)$ in Fig. 13, such that the notion that the Milgromian cluster might

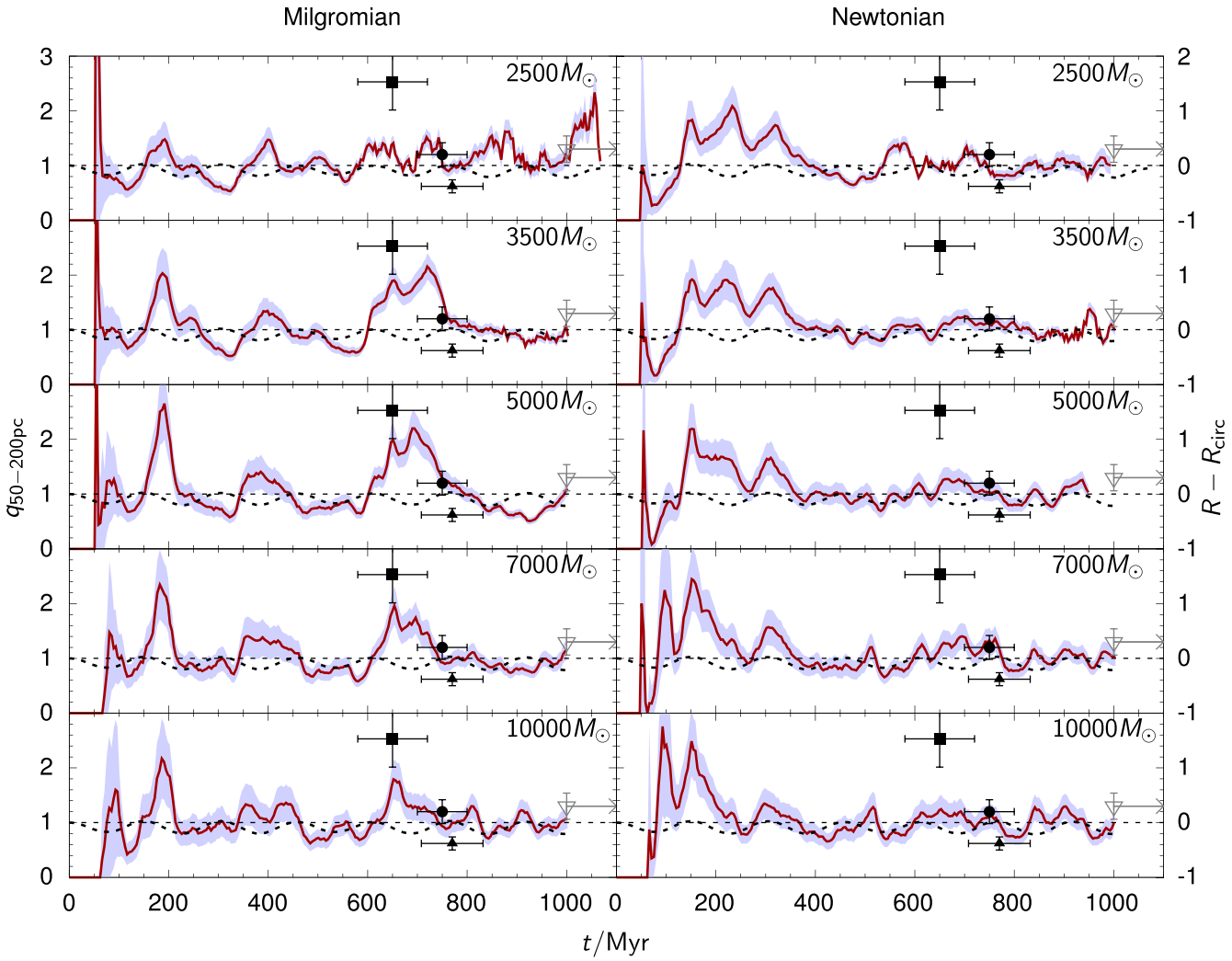

Figure 13. The number ratio, $q_{50-200\,\mathrm{pc}}(t)$, for five Milgromian (left-hand panels) and five Newtonian (right-hand panels) models as a function of time. The horizontal dashed line marks $q_{50-200\,\mathrm{pc}}(t) = 1$ (values >1 correspond to more stars in the front tail while values <1 correspond to the trailing tail having more stars, i.e. the dashed horizontal line is a marker for perfect symmetry in both tails for the left y-axis, and marks the Galactocentric radius of a circular orbit at 8.3 kpc for the right y-axis) and the initial masses, $M_{\mathrm{oc},0}$ are written into the panels. The shaded region corresponds to the Poisson 1 σ uncertainty range at each time. The data for the four open clusters listed in Table 1, for which the extended tidal tails have been extracted using *Gaia* eDR3 with the Jerabkova-CCP method (Section 2.2) are shown as the symbols (square: Hyades, circle: Coma Berenices, triangle: Praesepe, upside down open triangle: NGC 752). For each cluster, the error-bar on $q_{50-200\,\mathrm{pc}}$ is the 1 σ Poisson uncertainty and the error-bar on the age is the age range given in Table 1 except for NGC 752, which has an age of ≈1.75 Gyr not reached by the present simulations. For NGC 752, $q_{50-130\,\mathrm{pc}}$ is shown. Note that the Newtonian models fluctuate erratically around the value of $q_{50-200\,\mathrm{pc}}(t) \approx 1$ while the Milgromian models show quasi-periodic excursions to $q_{50-200\,\mathrm{pc}}(t) > 1$ and $q_{50-200\,\mathrm{pc}}(t) < 1$ with maxima near perigalacticon. The dotted line is the galactocentric distance in kpc ($R = |^{\mathrm{j}=6}\vec{R}|$, equation 22) relative to a circular orbit at $R_{\mathrm{circ}} = 8.3$ kpc. The model cluster orbits thus have apo-galactica at ≈8.3 kpc and peri-galactica at ≈8.1 kpc. The model clusters are on approximate rosette orbits such that the apo-galactica are <360° distant from each other and occur about every 150 Myr while the orbital period is about 209 Myr (Fig. 4). The computations indicate that the Milgromian models show a pronounced asymmetry in the tidal tails when the model clusters are near peri-galacticon.

experience an internal kinematically instability cannot, herewith, be affirmed.

The specific angular momentum per stellar particle for particles within the initial tidal radius, $r_{\mathrm{tid},0}$ (equation 20), of their model cluster centre is calculated as

$$\vec{L}_{/n} = \frac{1}{n_{\mathrm{tid}}} \left(\sum_{\mathrm{i}=1}^{n_{\mathrm{tid}}} \vec{r}_{\mathrm{i}} \times \vec{v}_{\mathrm{i}} \right), \tag{24}$$

where $\vec{r}_{\mathrm{i}}$, $\vec{v}_{\mathrm{i}}$ are, respectively, the position and velocity vectors of particle i relative to the model cluster's centre. The Z-axis points towards the galactic north pole and the model clusters orbit anticlockwise about the galactic centre. The specific inner angular momentum per particle of a model, $\vec{L}_{/n2}$, is calculated for all particles within half of r_{tid}.

The temporal evolution of the components of $\vec{L}_{/n}$ is plotted in Fig. 15. It is evident that the models are initially non-rotating, but that rotation develops with the loss of stellar particles. The Newtonian and Milgromian models follow a similar evolution. All models spin-up rapdily within the first ≈100 Myr due to the inital settling phase into the galactic potential which is associated with enhanced loss of particles.

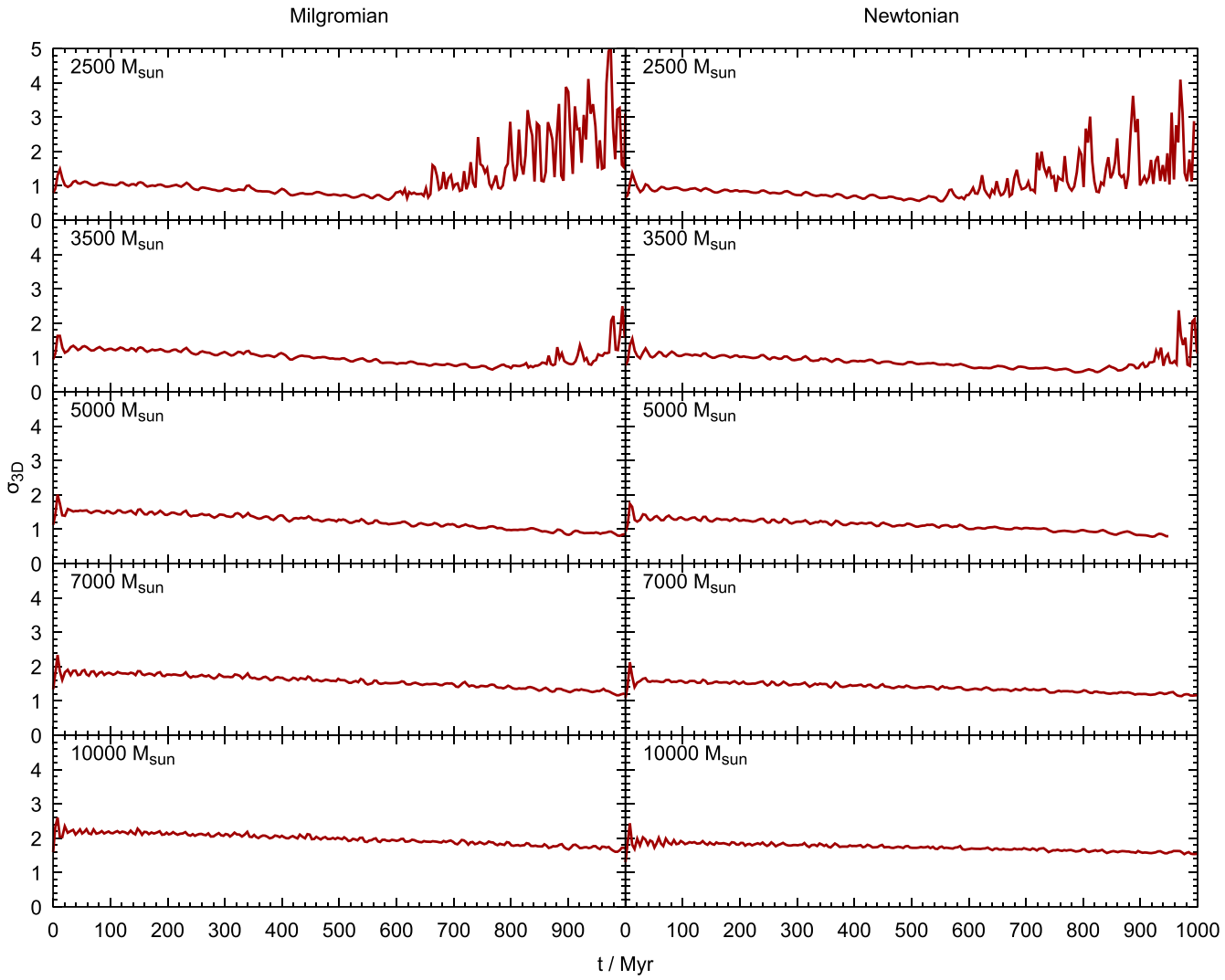

Figure 14. As Fig. 13 but plotting (w/o the Poisson uncertainties) the 3D velocity dispersion of particles within the initial tidal radius (equation 23). The velocity dispersion decreases as the models loose particles and the initially lighter models show erratic fluctuations in $\sigma_{3D}(t)$ after they have largely dissolved.

This spin-up of initially not-rotating open clusters that fill their tidal radii is well understood and has been found to be the case also for the evolution of the Milky Way satellite galaxies (Kroupa 1997): The escaping stellar particles preferably stem from the pro-grade population within the cluster as this is energetically favoured (Henon 1970; Read et al. 2006). An unbound star on a pro-grade cluster-centric orbit experiences a smaller tidal radius than other stars. It may overtake the cluster slightly but by retarding from it towards a larger galactocentric distance it will fall behind and populate the trailing tail. If it transits the práh near the inner Lagrange point at smaller galactocentric distance it will initially fall behind the cluster but will move ahead of it due to the increasing angular orbital frequency with smaller galactocentric distance, populating the leading tail. This pro-grade population can be re-populated after its loss from the cluster through artificial grid-relaxation in the models here and two-body relaxation in real clusters. From Fig. 15, it can be seen that the Milgromian models have a faster spin-up which continues over time, while the Newtonian models show a near negligible rise in the spin after the the first ≈100 Myr. This indicates that artificial grid relaxation is negligible (the Newtonian models do not re-populate their pro-grade stellar population significantly at the expense of the retrograde population) confirming the collision-less nature of these models. That the Milgromian models continue to spin-up over time (the blue lines have a small positive gradient) indicates that another process is at work that re-populates the pro-grade population within the models at the expense of the retro-grade orbits, and that this process accelerates. It needs to accelerate because the pro-grade population needs to be lost more rapidly than the retrograde population is depleted into the pro-grade one in order for the cluster spin to increase. Since the equivalent Newtonian models rule out artificial grid relaxation to be significant, this process is probably related to the precession of stellar orbits within the Milgromian clusters through the external field.

Indeed, in Milgromian gravitation, the EF leads to a star's orbit within the EF-dominated cluster to be torqued and thus to precess with the rate $\dot{\Omega}$. An estimate of the precession rate can be obtained by adapting equation (34) in Banik et al. (2020), although it is not clear that it is fully applicable to the present fully EF-dominated case,

$$\dot{\Omega} = \frac{f_{\rm g}\, G\, M_{\rm oc}\, a_0\, r_{\rm st}\, \sin(\theta)\cos(\theta)}{2\, v_{\rm st}\, r_{\rm efe}^3}. \qquad (25)$$

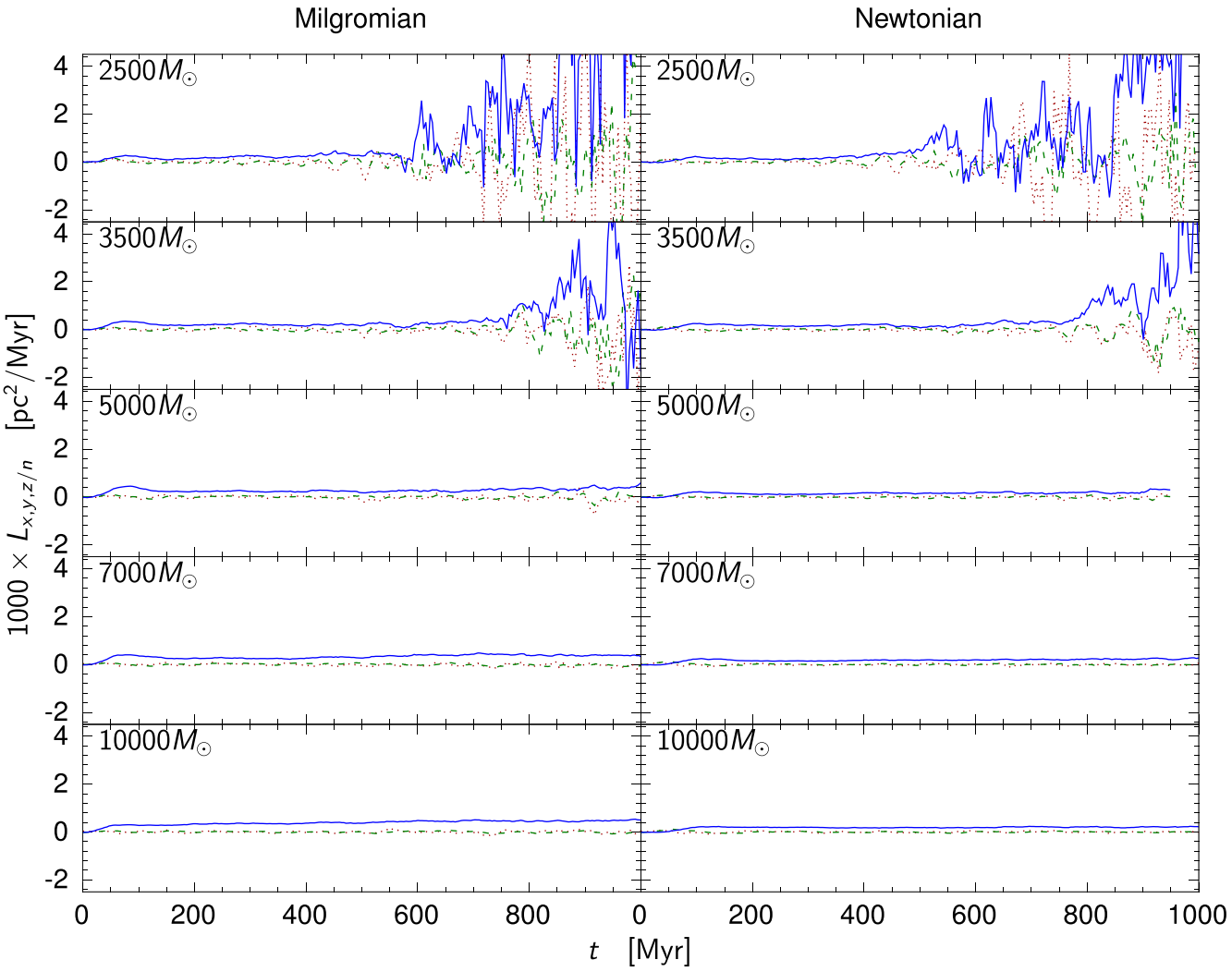

Figure 15. As Fig. 13 but plotting (w/o the Poisson uncertainties) the X- (dotted red line), the Y- (dashed green line), and the Z-component (solid blue line) of the time-evolution of the cluster's specific spin angular momentum per particle, $\bar{L}/n$ (equation 24, using all particles within the initial $r_{\rm tid}$ of each model). A positive Z-component is antiparallel to the angular momentum of the cluster's orbit around the Galaxy. Note that the Milgromian models typically have larger spins which is consistent with their larger mass loss and the argument of cluster spin-up in Section 5.4. The time-derivative of $L_{z/n}$ is plotted in Fig. 16.

Assuming $M_{\rm oc} = 275\,{\rm M}_\odot$, its $r_{\rm efe} \approx 0.29\,{\rm pc}$ (equation 31 in Banik et al. 2020: $r_{\rm efe} = \sqrt{G\,a_0\,M_{\rm oc}}/a_{\rm ext,kin}$ is the radius in the cluster beyond which the EF dominates; $a_{\rm ext,kin} \approx 7.5\,{\rm pc\,Myr^{-2}}$ from Table 1), the inclination between the direction of the EF and the orbital angular momentum of the star in the cluster, $\theta = 45^{\rm o}$, maximizes the sin-cos product, and $f_{\rm g} = 1/2$ is a geometric factor that accounts for azimuthal averaging. Equation (25) suggests a precession rate of $\approx$240 rad Myr^{-1} for a star at $r_{\rm st} = 5\,{\rm pc}$ moving with a circular speed of $v_{\rm st} = 0.5\,{\rm pc\,Myr^{-1}}$. This is extremely rapid, implying a precession-induced orbital instability. Note that

$$\dot{\Omega} \propto M_{\rm oc}^{-0.5}, \tag{26}$$

such that the precession speeds up as the cluster looses mass. This may be the reason for the increasing spin of the Milgromian models noted above. Also,

$$\dot{\Omega} \propto a_{\rm ext,kin}^{3}, \tag{27}$$

suggests that the process of precession of cluster-centric stellar orbits increases significantly at peri-galacticon, such that the evaporation rate may be more sensitive to the orbital eccentricity of the open cluster in Milgromian than in Newtonian gravitation.

The above estimate for $\dot{\Omega}$ is rough and other stars will experience significantly different precession rates, but it indicates that the EF is likely to have a highly significant systematic effect on the orbital structures and orbital angular momenta orientations of stars in an open cluster and may thus constitute an additional important contribution to the energy-redistribution process in Milgromian gravitation. This *EF-relaxation process* demands further investigation as it should also be important in globular clusters.

Every star cluster on a near-circular galactocentric orbit that is older than $t \approx 100\,{\rm Myr}$ (conservatively 200 Myr), that had revirialized after gas expulsion with a negligible spin (but see Mapelli 2017 for models of forming rotating clusters and Hénault-Brunet et al. 2012 for observational evidence for rotation in a very young massive cluster) will thus spin-up to rotate with a spin oppositely directed to

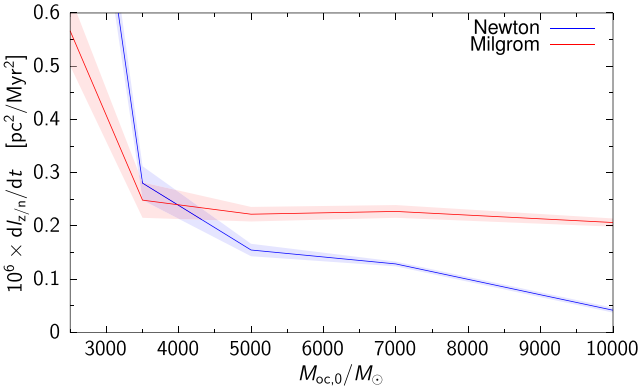

Figure 16. The rate of change of the Z-component of the specific spin angular momentum per particle of the model clusters, $dL_{z/n}/dt$, in dependence of the initial model mass, $M_{oc,0}$, for all particles within the initial tidal radius. The shaded regions corresponding to the $1\,\sigma$ uncertainty in the linear fit to $L_{z/n}(t)$ (Fig. 15). For this purpose, the linear fit is restricted to the following time intervals: 200–500 Myr ($M_{oc,0} = 2500M_\odot$), 200–750 Myr ($M_{oc,0} = 3500M_\odot$), 200–1000 Myr ($M_{oc,0} > 3500M_\odot$). Fig. 17 shows the time derivative of $L_{z,/n2}$ for particles within half the tidal radius.

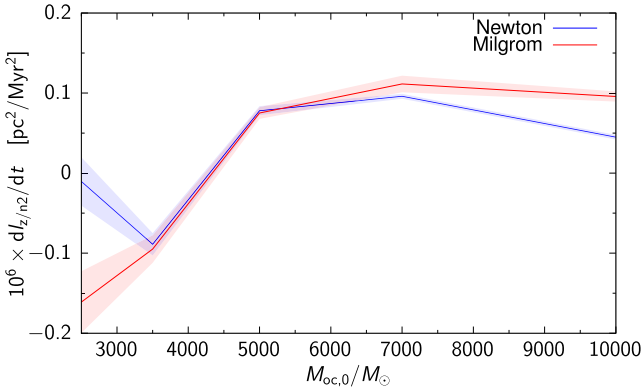

Figure 17. As Fig. 16 but for all particles within half the initial tidal radius.

its orbital angular momentum around the galactic centre.[10] This is shown in Fig. 15 in that the Z-component of $\vec{L}_{/n}$, $L_{z/n}$, increases and is positive while the orbital angular momentum of the cluster about the Galaxy is directed towards the negative Z -direction: if the initially non-rotating open cluster orbits the Galaxy in an anti-clockwise direction, then the open cluster will begin to rotate clockwise.

According to Fig. 15, the evolution of $\vec{L}_{/n}$ does not show fluctuations that would support the notion that correlated particle motions lead to the near-periodic increases and decreases of $q_{50-200\,pc}(t)$. The rate of change of $L_{z/n}(t)$ and of $L_{z/n2}(t)$ (using only particles within half of the initial r_{tid}) are plotted in Fig. 16 and 17, respectively. The models with $M_{oc,0} \lesssim 4000M_\odot$ are barely resolved given the small density contrast of the cluster relative to the field, and the more reliable more massive models indicate that the Milgromian clusters keep spinning up at a constant rate, $dL_{z/n}/dt \approx 0.22 \times 10^{-6}$ pc^2 Myr^{-2}, independently of their initial mass (similarly for the inner part), while the Newtonian models experience a significantly smaller spin-up over time which decreases with increasing model mass (see Tiongco et al. 2016 for an in-depth n-body study). Given the explorative and grid-based approximative nature of this work, we do not further analyse the rate of spin-up in relation to cluster mass loss rate.

The explorative calculations performed so far show Milgromian models to preferentially loose stars across their práhs through the leading tidal tail. This leads to them spinning up with time (Fig. 15) and also leads to growth of their orbital eccentricity (equation 2) since the clusters decelerate through this one-sided out-sourcing of their stars. The initial orbital eccentricities of the present models are $e \approx 0.012$, and using the method of Appendix A to calculate the momentary value of $e(t) = e_{snap}$ from the position and velocity vectors of the model centres (equation A1), the time evolution of $e_{snap}(t)$ can be studied.

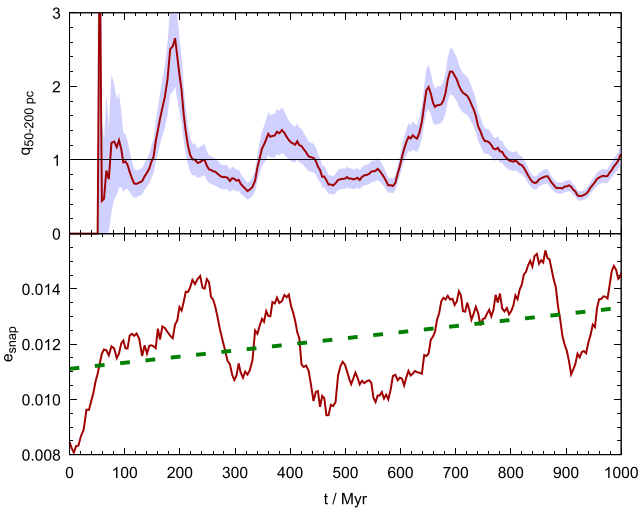

Figure 18. The evolution of the orbital eccentricity, $e_{snap}(t)$, of the Milgromian model with $M_{oc,0} = 5000M_\odot$ (lower panel) in comparison with the evolution of $q_{50-200\,pc}(t)$ (upper panel, same as in Fig. 13). The orbital eccentricity varies as $q_{50-200\,pc}$ does, but is retarded by about 40 Myr for the first two maxima. The dashed line shows the overall linear trend of $e_{snap}(t)$.

The evolution of $e_{snap}(t)$ is shown for the Milgromian model with $M_{oc,0} = 5000M_\odot$ in Fig. 18. It is evident that, when the model looses more stars across its práh into the leading tail, then e_{snap} increases as a consequence of the loss of momentum of the cluster, while, when the trailing tail receives more stars, e_{snap} decreases again. Due to the time-averaged asymmetry the clusters loose more stars into the leading tail (Fig. 9, 11, and 12), and thus continuously decelerate therewith steadily increasing their overall $e(t)$ with time.

While the Newtonian models approximately retain their initial orbital eccentricity, the Milgromian models thus show an approximately linearly increasing $e_{snap}(t)$. By performing a linear regression on the $e_{snap}(t)$ data (as shown for example in Fig. 18), the gradient, de_{snap}/dt is evaluated and shown in Fig. 19. Interestingly,

[10]Globular clusters are typically on chaotic rosette-type orbits about the Galactic centre such that their spins are not likely to be well correlated with their Galactocentric orbital angular momenta. The interested reader is referred to the comprehensive Newtonian n-body study of rotating globular clusters by Tiongco, Vesperini & Varri (2016, 2017, 2018, 2022), Tiongco, Collier & Varri (2021). Bianchini et al. (2018) find significant evidence for a non-negligible spin of 11 out of 51 globular clusters but do not place this in relation to the orbital angular momentum of the clusters. Sollima (2020) analyses Gaia-selected member stars around 18 globular clusters, finding evidence for tidal tails in seven of them with five having asymmetric tails (the directions of motion of the clusters are not given though). This asymmetry may be related to the asymmetry discussed here, but is likely affected significantly by the eccentricities of the cluster orbits. Flat outer velocity dispersion profiles around some globular clusters have been reported (Scarpa et al. 2011).

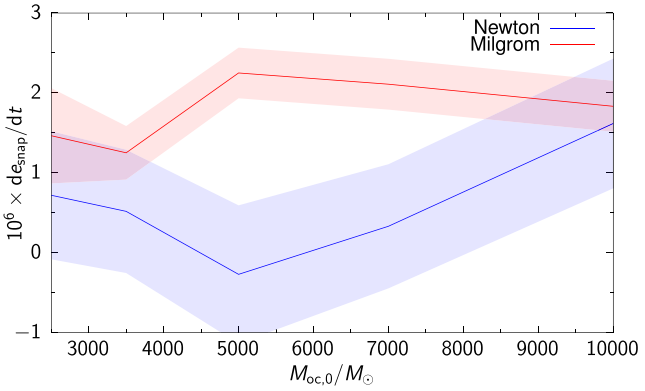

Figure 19. The rate of change of the orbital eccentricity in dependence of the initial model mass, $M_{oc,0}$. The shaded regions correspond to the $1\,\sigma$ uncertainty in the linear fit to $e_{sn}(t)$.

the Milgromian models have a similar time-gradient $de_{snap}/dt \approx 1.8 \times 10^{-6}\,\mathrm{Myr}^{-1}$ at more than $5\,\sigma$ confidence, while the Newtonian models have a gradient consistent within $2\,\sigma$ with zero. The present Milgromian models thus increase their orbital eccentricity by 20 per cent over a time of 1 Gyr.

This confirms the supposition that the one-sided loss of stars decelerates the Milgromian models such that their orbital eccentricity increases with time. A more detailed analysis of this problem is beyond this explorative study, given the limited access to computational resources, and is relegated to a follow-up study. This explorative work does, however, suggest that in Milgromian dynamics open star clusters would self-destroy as they spin-up. The asymmetrical loss of stars dominantly into the leading tail leads to a deceleration of the cluster, a decreasing peri-Galacticon, which increases the asymmetrical loss to a potentially catastrophic level as the process appears to be subject to positive dynamical feedback. Clearly, further research on this process of open-cluster suicide is needed to reach more secure conclusions.

5.5 Emergence from molecular cloud and lifetimes

In Milgromian gravitation, galactic discs have a stronger self-gravitation than in Newtonian plus dark-matter-halo models, leading to an enhanced star-formation rate per unit gas mass and also to star-formation extending to larger galactocentric radii (Zonoozi et al. 2021). The emergence of star clusters from their molecular clouds of birth involves a phase transition from the Newtonian deeply embedded cluster phase to the Milgromian open cluster configuration.

From the half-mass radius–embedded-cluster mass-in-stars relation, $r_h/\mathrm{pc} = 0.10\,(M_{ecl}/\mathrm{M}_\odot)^{0.13}$ (Marks & Kroupa 2012), it follows, together with equation (13), that $r_M > r_h$ for $M_{ecl} > 4\mathrm{M}_\odot$ for a star-formation efficiency of 33 per cent. It is interesting to note that $M_{ecl} \approx 5\mathrm{M}_\odot$ corresponds to the least-massive embedded clusters that are observed in nearby molecular clouds (Kroupa & Bouvier 2003; Joncour et al. 2018). This also means that the precursors of all open and globular star clusters form in the Newtonian regime. But, the least-massive embedded clusters have a MOND radius comparable to their half-mass radius, suggesting they would form in the EF-dominated Milgromian gravitational regime, i.e. with an effectively larger gravitational constant, G_{eff}. The emergence from the natal molecular cloud and the re-virialization of a part of the embedded cluster will occur mostly in the Milgromian EF dominated spatially asymmetrical regime (Fig. 3) such that the presently known limits on bound fractions of this process (e.g. Boily & Kroupa 2003a,b; Brinkmann et al. 2017; Farias et al. 2018; Domínguez et al. 2021) may need adjustment. This problem has been studied by Wu & Kroupa (2018) and Wu & Kroupa (2019) indicating the rich stellar-dynamical evolution and possible outcomes. A larger fraction of stars can remain bound to the freshly formed open cluster due to the larger G_{eff} with a reduced fraction of stars to be found in tidal tail I (Section 1) compared to Newtonian models. These processes will need future attention to better understand the kinematics and shapes of natal cocoons.

Observations of extragalactic open star clusters appear to show these to dissolve unexpectedly quickly (Fall & Chandar 2012; Chandar et al. 2017). The dissolution appears to be faster than expected from Newtonian n-body simulations in smooth galactic potentials (Dinnbier et al. 2022a). The lifetimes of real open clusters are subject to assumptions on their orbits, the IMF, binary fraction, their initial sizes and masses (e.g. Mapelli 2017; Ballone et al. 2020; González-Samaniego & Vazquez-Semadeni 2020; Ballone et al. 2021). The calculated models are thus degenerate to various combinations of the parameters (unless all open clusters form following the same mass-radius relation, the same IMF and initial binary population and the Galactic potential is smooth, cf. Marks & Kroupa 2012; Dinnbier et al. 2022a). Therefore, the reported *short lifetime problem* needs more research and should not, for the time being, be taken as conclusive evidence in the one or other direction. Given this situation, it is relevant to ask: Is it possible that Milgromian open clusters dissolve faster than Newtonian ones?

In Section 5.1, it was found that the particle-mesh Milgromian models dissolve more rapidly than the Newtonian models of the same mass due to Milgromian clusters becoming more unbound per unit mass loss. In addition to this general process, the energy-equipartition-driven stellar loss is likely to be faster for Milgromian clusters than for Newtonian clusters. Ciotti & Binney (2004) showed that the two-body relaxation time-scale is significantly shorter in Milgromian clusters, although reliable values are not available and their computation is only valid for clusters in isolation. Ignoring this (truly fundamental) limitation for the moment, we can compute the relaxation time ignoring the external field. The following two estimates can be made: The lifetime of a Newtonian open cluster (e.g. Binney & Tremaine 1987), $T_{diss,N} = \gamma\, t_{relax}$, where $\gamma \approx 19$ when the cluster is in the field of the Solar neighbourhood and t_{relax} is the median two-body relaxation time scale. According to Ciotti & Binney (2004), the ratio of the two-body relaxation time in Milgromian to Newtonian gravitation is

$$\frac{t_{relax,M}}{t_{relax,N}} = 1.4\,(1+\mathcal{R})^{-\nabla/\in}, \tag{28}$$

where $\mathcal{R} = (M_{oc,grav} - M_{oc})/M_{oc}$. For example, for the Hyades, $M_{oc} = 275\mathrm{M}_\odot$ is the stellar mass (Table 1) while the effective-Newtonian gravitational mass is about a factor of four larger (Röser et al. 2011). Thus, for the Hyades, $t_{relax,M}/t_{relax,N} \approx 0.044$ such that Milgromian open clusters would dissolve about 23 times more rapidly than Newtonian ones (taking the Hyades as representative). A twenty-fold shortening of the life-times is ruled out by the observation that Hyades-type clusters with a birth mass near $1300\,\mathrm{M}_\odot$ (Jerabkova et al. 2021) have life-times longer than 600 Myr while the Newtonian expectation is 2 Gyr (Section 2.1). The empirical evidence suggests a shortening at most by not much more than a factor of two.

Another estimate can be obtained by remembering that $t_{relax,N} \approx (2\,N/\ln(N/2))\,t_{cross}$, where $t_{cross} = 2\,r_h/\sigma_{3D}$ is the half-mass crossing time. If the boost in velocity dispersion is only 25 per cent using the EF-dominated MOND estimates (Section 5.1), then the lifetimes

would be shorter by only about 20 per cent. Assuming that, for some yet unknown reasons, the collisional treatment would reproduce the observed velocity dispersion, then the relaxation time and thus the lifetime would be reduced by a factor of two for the Hyades.

Another estimate for the shortening of the lifetimes of Milgromian versus Newtonian clusters can be obtained as follows: the lifetime of a Newtonian cluster, $T_{\rm diss,N}$, is given by equation (1). As noted in Section 5.1, open clusters are in the EF-dominated regime such that they follow Newtonian dynamics. If $T_{\rm diss,M}$ is the lifetime of the Milgromian cluster, then $T_{\rm diss,M}/T_{\rm diss,N} = (G/G_{\rm eff})^{1/2} = \sqrt{\mu} \approx 0.8$ (equation 17). This estimate thus implies EF-dominated clusters to have a lifetime which is about 80 per cent that of the corresponding Newtonian cases.

The above estimates thus indicate that the lifetimes of open clusters in Milgromian gravitation are between 20 to 50 per cent of those in Newtonian gravitation. It remains to be studied how star-cluster populations evolve in a Milgromian galaxy, noting that observational evidence suggests that the dissolution rate of star clusters may be independent of their mass (Fall & Chandar 2012; Chandar et al. 2017). From the results of Section 5.1, it is tentatively suggested that $t_{\rm life,M}/t_{\rm life,N} \approx 7.4\,(M_{\rm oc}/{\rm M}_\odot)^{-0.25}$. While the lifetimes of Newtonian star clusters in the Solar neighbourhood lengthen with increasing $M_{\rm oc}$ due to the increasing two-body relaxation time approximately according to $T_{\rm diss} \propto M_{\rm oc}^{0.79}$ (equation 1), this suggests that the lifetimes of EF-dominated Milgromian clusters may at the same time be reduced due to the larger loss in binding energy per unit mass loss. The combination of these two effects may lead to life-times of EF-dominated star clusters being less-dependent on the cluster mass, $t_{\rm life,M} \overset{\propto}{\sim} (M_{\rm oc})^{0.5}$.

The rapidity with which open clusters dissolve is dependent on how quickly the orbital energies of the stars in the cluster are redistributed through weak gravitational encounters. The observation in Section 5.4 that the Milgromian models spin-up over time while the Newtonian ones do not may indicate another contribution to the more rapid dissolution of Milgromian clusters: the rapid precession of stellar orbits in Milgromian clusters leads to a more rapid depopulation of the cluster-centric retro-grade orbits which precess into pro-grade orbits that are preferentially lost. This process accelerates with time (equation 26) as the cluster's mass decreases, leading to cluster suicide.

For completeness, further results on the richness of the Milgromian gravitational dynamics of open star clusters, globular clusters, and dwarf galaxies can be found in Brada & Milgrom (2000) who study the dynamical influence of the EF on orbiting satellite galaxies. Thus the asymmetry of an ultra-diffuse dwarf galaxy's potential (see Fig. 3) will affect the morphology of its tidal features with implications for the interpretation of its dark matter content in Newtonian gravitation (cases in point being the dark-matter-lacking dwarf galaxies NGC 1052-DF2/DF4, Famaey, McGaugh & Milgrom 2018; Kroupa et al. 2018; Keim et al. 2022; Montes et al. 2021). Wu & Kroupa (2013) analyse the phase transition a massive star cluster experiences on a radial orbit when moving from the Newtonian into the outer Milgromian regime, and Thomas et al. (2018) demonstrate that the asymmetry of a cluster's potential leads to asymmetrically long tidal tails II explaining the unequal lengths of the observed tidal tails of the globular cluster Palomar 5.

6 SUMMARY AND CONCLUSION

Twenty per cent to a half of all stars in a galaxy pass through a classical tidal tail II which is fed through the evaporation process of their star cluster of origin. The remainder are lost from their embedded clusters through gas expulsion forming, together with the stars from other embedded clusters that formed in the same molecular cloud, dispersing natal cocoons about individual revirialized open clusters. After ≈200 Myr, the classical tidal tail II becomes the dominant coeval population within a few hundred pc of the open cluster. In Newtonian dynamics and for a smooth galactic potential, the stars cross the práh of their cluster symmetrically at the inner and outer Lagrange points leading to symmetrical classical tidal tails within Poisson noise (Pflamm-Altenburg et al., in preparation). But for all open clusters for which tail data are available the leading tail contains more stars than the trailing tail within a cluster-centric distance of $d_{\rm cl} \approx 50$ pc (Section 2.2).

With the introduction of the compact convergent point method by Jerabkova et al. (2021), it has now become possible to map-out the extended ($d_{\rm cl} > 50$ pc) phase-space distribution of coeval stars in the classical tidal tail II around nearby open clusters using *Gaia* eDR3. In the case of the Hyades, the tidal tail is asymmetrical with the leading tail containing significantly more stars than the trailing tail (Fig. 2). This was interpreted by Jerabkova et al. (2021) to possibly be due to a recent encounter with a massive perturber, which would have damaged the trailing tail, thereby also leading to dynamical heating of the Hyades which would consequently dissolve within a few cluster crossing times. This is consistent with the observed super-virial state of the real cluster (a factor of four missing in mass assuming Newtonian gravitation, Röser et al. 2011; Oh & Evans 2020). A problem with this scenario is that the Sun and Hyades are in the Local Bubble such that a sufficiently massive molecular cloud does not exist nearby to the Hyades and the existence of dark matter subhaloes remains to be speculative (Section 2.3). Furthermore, about three times older open cluster NGC 752 shows a comparable, albeit much less significant, asymmetry (Boffin et al. 2022, Fig. 13) requiring a similar encounter, making this explanation unlikely.

Can the asymmetry in the tidal tails be explained if gravitation is Milgromian rather than Newtonian? Milgrom (1983) noted that the open star clusters would be in the Milgromian regime with their internal gravitational forces being dominated by the external field from the Galaxy (Section 3.2.2). The work of Wu et al. (2008), Wu et al. (2010) and Wu et al. (2017) showed the equipotential surfaces of satellites (dwarf galaxies or star clusters) to be lopsided in Milgromian gravitation, therewith breaking the symmetry between the inner and outer Lagrange points. A star moving away from the centre of its hosting cluster will experience a larger radial backwards force when moving away from the galactic centre (Fig. 3). This may be the reason for the number of stars in the leading tidal tail being larger than in the trailing tail for $d_{\rm cl} \lesssim 50$ pc for all five clusters for which tail data exist (Section 2.2). But, the older open cluster Coma Berenices has a nearly symmetrical tidal tail in the distance range $50 < d_{\rm cl}/{\rm pc} < 200$ while the Praesepe has slightly fewer stars in the leading tail in this same distance range from the cluster (Fig. 13). This appears to contradict a Milgromian interpretation of the data without salving the disagreement with Newtonian gravitation for $d_{\rm cl} \lesssim 50$ pc for all five clusters and for $d_{\rm cl} > 50$ pc for the Hyades and NGC 752.

Given the non-existence of a relaxational Milgromian *n*-body code, the symmetry-problem of tidal tails is here approached by applying the existing collision-less adaptive-mesh refinement PoR code (Section 5) to follow how stellar particles leak across the práh of their model cluster. The equivalent Newtonian computations verify that the tails are largely symmetrical, while the Milgromian calculations demonstrate them to be significantly asymmetrical. This confirms the expectation that a Milgromian star cluster orbiting the

Galaxy on a near-circular orbit in the MW disc looses more stars through the leading tidal tail (Section 5.2).

The calculations show the ratio between the number of stellar particles in the leading to the trailing tail to oscillate near-periodically, reaching the high-observed values of the Hyades and decreasing to the Newtonian symmetry reaching a small but reversed asymmetry (Fig. 13). The maximum asymmetry is reached when the models are near peri-galacticon while the asymmetry nearly disappears at apo-galacticon. The observed tidal tails of the Hyades, Coma Berenices, and the Praesepe appear to follow the theoretical time evolution of the asymmetry ratio (Fig. 13). While the asymmetry and ages of the models and real clusters agree, it is not clear if the real Hyades and NGC 752 are in periastron, and if Coma Ber and Praesepe are near apo-galacticon. An interesting problem to consider would be to search for a Galactic potential which places the Hyades and NGC 752 near peri-galacticon and Coma Ber and the Praesepe near apo-galacticon, given the observational constraint on their velocity vectors. In future work, the contribution from the Galactic bar needs to be taken into account as well as orbital oscillations about the Galactic mid-plane.

The calculations performed for this explorative study indicate a possible physical mechanism for the oscillating behaviour of the 50–200 pc tail asymmetry. While the Newtonian models retain an approximately constant orbital eccentricity, it grows with time for the Milgromian models because these loose more stars across their práh into the leading tail than the trailing tail. The physical process of the loss of stars (Section 5.4) may be driven by the rapid precession of stellar orbits within the cluster due to the EF, leading to an increasingly rapid EF-relaxational redistribution of orbits as the cluster looses mass, therewith growing the orbital eccentricity. This process, if true, would accelerate cluster death.

A prediction of this work is that open star clusters that are initially non-rotating and older than about 200 Myr show a spin which is opposite to the orbital angular momentum of the cluster (Section 5.4). Another prediction is that in Milgromian gravitation the first Küpper epicyclic overdensity lies further from the cluster in the leading tail than the trailing tail, both being more distant from the cluster centre than in Newtonian dynamics (Section 5.1).

The estimates in Section 5.5 suggest Milgromian open clusters to have life times that are 20–50 per cent of those of Newtonian open clusters of the same initial mass because the two-body relaxation process is faster. This may have a bearing upon the observation (Fall & Chandar 2012) that open clusters appear to dissolve more rapidly than expected from Newtonian n-body computations.

In the future, it will be important to verify and better measure the tidal tails for open star clusters covering a larger range of ages. This will allow an elaboration on the present findings and an assessment of the evaporation rate of stars into the leading and trailing tidal tails as well as the measurement of the locations of the Küpper epicyclic overdensities as more refined tests of Milgromian gravitation. Given the present results based on a collision-less method and the result that two-body relation is much more significant in Milgromian systems than in Newtonian ones (Ciotti & Binney 2004), and to achieve theoretical advances, it will be necessary to develop a collisional n-body code in Milgromian gravitation to allow open star clusters to be evolved self-consistently. This is a very major mathematical and computational challenge with currently no clear solution in sight. An ansatz could be to discretize the generalized Poisson equation (Section 3.1) and possibly to use an iterative procedure to calculate the instantaneous effective-Newtonian gravitational mass of each star in the cluster, and/or to just use the original definition of the MONDian force equation (Milgrom 1983) with the usual particle summation over the $particle\text{-}distance^{-2}$ mass terms (Pflamm-Altenburg, in preparation). Close encounters between stars and multiple systems and their perturbations will need to be treated according to regularization methods (Heggie 1974; Mikkola & Aarseth 1990, 1993; Funato et al. 1996; Mikkola & Aarseth 1996) and stellar-evolution will need to be implemented through fast look-up tables (Hurley, Pols & Tout 2000; Hurley, Tout & Pols 2002; Banerjee et al. 2020). The discs of galaxies are entirely self-gravitating in MOND, enhancing the star-formation rate, as opposed to the Newtonian case where the dark matter halo dominates the potential (Zonoozi et al. 2021). A Milgromian n-body simulation code will be mandatory to address the emergence through gas expulsion of open and globular clusters from their deeply-embedded Newtonian state (Section 5.5), the rate with which stars mass-segregate and evaporate, how long open star clusters live and how their orbits evolve.

Gravitation remains the least-understood physical phenomenon. Different interpretations of this phenomenon have been proposed as a geometrical distortion of space-time through matter (Einstein 1916), as an emergent property related to the information content of space (Verlinde 2011), or it being related to the wave-nature of particles (Stadtler, Kroupa & Schmid 2021). The present contribution suggests that departures at low accelerations from Newtonian/Einstein gravitation might be already evident on the pc-scale. To advance our understanding of this phenomenon, it will be important to achieve more direct tests on the sub-pc scale. Three methods have been proposed to achieve headway:

(i) Using very wide binary systems to test the law of gravitation (Hernandez, Jiménez & Allen 2012; Scarpa et al. 2017; Banik, Pittordis & Sutherland 2021; Pittordis & Sutherland 2022, but see Clarke 2020; Loeb 2022a).

(ii) Tracking the orbital motion of Proxima Cen with high-precision astrometry to uncover the expected Milgromian departures from the Newtonian trajectory (Banik & Kroupa 2019a).

(iii) Using an ensemble of small space craft to map out the acceleration field surrounding the Sun which will allow to detect the Milgromian departures from the Newtonian force law on the scale of the outer Solar System (Banik & Kroupa 2019b).

ACKNOWLEDGEMENTS

We thank an anonymous referee for very helpful suggestions, and František Dinnbier for useful comments. Tereza Jerabkova was an ESA Research Fellow when this work was begun. Jörg Dabringhausen, Jaroslav Haas, Pavel Kroupa, and Ladislav Šubr acknowledge support through the Grant Agency of the Czech Republic under grant number 20-21855S and the DAAD-East-European-Exchange programme at the University of Bonn. Benoit Famaey acknowledges funding from the Agence Nationale de la Recherche (ANR projects ANR-18- CE31-0006 and ANR-19-CE31-0017), and from the European Research Council (ERC) under the European Union's Horizon 2020 Framework programme (grant agreement number 834148). Guillaume Thomas acknowledges support from the Agencia Estatal de Investigación (AEI) of the Ministerio de Ciencia e Innovación (MCINN) under grant FJC2018-037323-I. The restaurant Havelská Koruna ('knedlíkarna') in Prague was an essential location throughout this work – Knedlíkům zdar!

The word 'práh' means threshold in Czech. Prague ('Praha' in Czech) derives its mythological name from práh alluding to the location being the threshold to another world: on princess Libuše having a vision of a great new city at the Vltava, Praha was founded

with the práh to a new house. We use this as a general term referring to the true tidal threshold instead of calling it the 'Jacobi radius', which is only an approximation for perfectly circular orbits.

DATA AVAILABILITY

The results are based on calculated models and the observational data are available as described within this manuscript.

REFERENCES

Aarseth S. J., 1999, PASP, 111, 1333
Aarseth S. J., 2010, Gravitational N-Body Simulations. Cambridge Univ. Press, Cambridge
Aarseth S. J., Henon M., Wielen R., 1974, A&A, 37, 183
Aarseth S. J., Tout C. A., Mardling R. A., 2008, Lecture Notes in Physics, Vol. 760, The Cambridge N-Body Lectures. Springer-Verlag, Berlin, Heidelberg
Allen C., Santillan A., 1991, RMxAA, 22, 255
Angelo M. S., Santos J. F. C., Corradi W. J. B., Maia F. F. S., 2019, A&A, 624, A8
Armstrong J. J., Wright N. J., Jeffries R. D., Jackson R. J., Cantat-Gaudin T., 2022, preprint (arXiv:2208.05277)
Asencio E., Banik I., Mieske S., Venhola A., Kroupa P., Zhao H., 2022, MNRAS, 515, 2981
Bai L., Zhong J., Chen L., Li J., Hou J., 2022, Res. Astron. Astrophys., 22, 055022
Ballone A., Mapelli M., Di Carlo U. N., Torniamenti S., Spera M., Rastello S., 2020, MNRAS, 496, 49
Ballone A., Torniamenti S., Mapelli M., Di Carlo U. N., Spera M., Rastello S., Gaspari N., Iorio G., 2021, MNRAS, 501, 2920
Banerjee S., Kroupa P., 2011, ApJ, 741, L12
Banerjee S., Kroupa P., 2017, A&A, 597, A28
Banerjee S., Belczynski K., Fryer C. L., Berczik P., Hurley J. R., Spurzem R., Wang L., 2020, A&A, 639, A41
Banik I., Kroupa P., 2019a, MNRAS, 487, 1653
Banik I., Kroupa P., 2019b, MNRAS, 487, 2665
Banik I., Zhao H., 2022, Symmetry, 14, 1331
Banik I., Thies I., Famaey B., Candlish G., Kroupa P., Ibata R., 2020, ApJ, 905, 135
Banik I., Pittordis C., Sutherland W., 2021, preprint (arXiv:2109.03827)
Baumgardt H., Makino J., 2003, MNRAS, 340, 227
Baumgardt H., Hut P., Heggie D. C., 2002, MNRAS, 336, 1069
Baumgardt H., Grebel E. K., Kroupa P., 2005, MNRAS, 359, L1
Beccari G., Boffin H. M. J., Jerabkova T., 2020, MNRAS, 491, 2205
Bekenstein J., Milgrom M., 1984, ApJ, 286, 7
Bianchini P., van der Marel R. P., del Pino A., Watkins L. L., Bellini A., Fardal M. A., Libralato M., Sills A., 2018, MNRAS, 481, 2125
Binney J., Tremaine S., 1987, Galactic dynamics. Princeton Univ. Press, Princeton, NJ
Boffin H. M. J., Jerabkova T., Beccari G., Wang L., 2022, MNRAS, 514, 3579
Boily C. M., Kroupa P., 2003a, MNRAS, 338, 665
Boily C. M., Kroupa P., 2003b, MNRAS, 338, 673
Bouma L. G., Curtis J. L., Hartman J. D., Winn J. N., Bakos G. Á., 2021, AJ, 162, 197
Brada R., Milgrom M., 2000, ApJ, 541, 556
Brinkmann N., Banerjee S., Motwani B., Kroupa P., 2017, A&A, 600, A49
Candlish G. N., Smith R., Fellhauer M., 2015, MNRAS, 446, 1060
Cantat-Gaudin T. et al., 2018, A&A, 618, A93
Carrera R. et al., 2022, A&A, 658, A14
Casertano S., Hut P., 1985, ApJ, 298, 80
Chae K.-H., Lelli F., Desmond H., McGaugh S. S., Li P., Schombert J. M., 2020, ApJ, 904, 51
Chae K.-H., Desmond H., Lelli F., McGaugh S. S., Schombert J. M., 2021, ApJ, 921, 104
Chandar R., Fall S. M., Whitmore B. C., Mulia A. J., 2017, ApJ, 849, 128
Chumak Y. O., Rastorguev A. S., 2006a, Astron. Lett., 32, 157
Chumak Y. O., Rastorguev A. S., 2006b, Astron. Lett., 32, 446
Ciotti L., Binney J., 2004, MNRAS, 351, 285
Clarke C. J., 2020, MNRAS, 491, L72
Dabringhausen J., Marks M., Kroupa P., 2022, MNRAS, 510, 413
de Bruijne J. H. J., 1999, MNRAS, 306, 381
de La Fuente Marcos R., 1998a, PASP, 110, 1117
de La Fuente Marcos R., 1998b, A&A, 333, L27
Derakhshani K., 2014, ApJ, 783, 48
Dias W. S., Monteiro H., Caetano T. C., Lépine J. R. D., Assafin M., Oliveira A. F., 2014, A&A, 564, A79
Dinnbier F., Kroupa P., 2020a, A&A, 640, A84
Dinnbier F., Kroupa P., 2020b, A&A, 640, A85
Dinnbier F., Walch S., 2020, MNRAS, 499, 748
Dinnbier F., Kroupa P., Anderson R. I., 2022a, A&A, 660, A61
Dinnbier F., Kroupa P., Šubr L., Jeřábková T., 2022b, ApJ, 925, 214
Djordjevic J. O., Thompson M. A., Urquhart J. S., Forbrich J., 2019, MNRAS, 487, 1057
Domínguez R., Farias J. P., Fellhauer M., Klessen R. S., 2021, MNRAS, 508, 5410
Einstein A., 1916, Ann. Phys., Lpz., 354, 769
Erkal D., Koposov S. E., Belokurov V., 2017, MNRAS, 470, 60
Ernst A., Just A., Berczik P., Olczak C., 2011, A&A, 536, A64
Fall S. M., Chandar R., 2012, ApJ, 752, 96
Famaey B., McGaugh S. S., 2012, Living Rev. Relativ., 15, 10
Famaey B., McGaugh S., Milgrom M., 2018, MNRAS, 480, 473
Farias J. P., Fellhauer M., Smith R., Domínguez R., Dabringhausen J., 2018, MNRAS, 476, 5341
Fellhauer M., Lin D. N. C., Bolte M., Aarseth S. J., Williams K. A., 2003, ApJ, 595, L53
Forbes D. A., Kroupa P., 2011, PASA, 28, 77
Fukushige T., Heggie D. C., 2000, MNRAS, 318, 753
Funato Y., Hut P., McMillan S., Makino J., 1996, AJ, 112, 1697
Fürnkranz V., Meingast S., Alves J., 2019, A&A, 624, L11
Gaia Collaboration, 2018, A&A, 616, A10
Gentile G., Famaey B., de Blok W. J. G., 2011, A&A, 527, A76
Gieles M., Sana H., Portegies Zwart S. F., 2010, MNRAS, 402, 1750
González-Samaniego A., Vazquez-Semadeni E., 2020, MNRAS, 499, 668
Haghi H., Baumgardt H., Kroupa P., Grebel E. K., Hilker M., Jordi K., 2009, MNRAS, 395, 1549
Haghi H., Zonoozi A. H., Kroupa P., Banerjee S., Baumgardt H., 2015, MNRAS, 454, 3872
Haghi H., Bazkiaei A. E., Zonoozi A. H., Kroupa P., 2016, MNRAS, 458, 4172
Haghi H. et al., 2019, MNRAS, 487, 2441
Hees A., Famaey B., Angus G. W., Gentile G., 2016, MNRAS, 455, 449
Heggie D. C., 1974, Celestial Mechanics, 10, 217
Heggie D., Hut P., 2003, The Gravitational Million-Body Problem: A Multidisciplinary Approach to Star Cluster Dynamics. Cambridge Univ. Press, Cambridge
Hénault-Brunet V. et al., 2012, A&A, 545, L1
Henon M., 1969, A&A, 2, 151
Henon M., 1970, A&A, 9, 24
Hernandez X., Jiménez M. A., Allen C., 2012, EPJ C, 72, 1884
Hurley J. R., Pols O. R., Tout C. A., 2000, MNRAS, 315, 543
Hurley J. R., Tout C. A., Pols O. R., 2002, MNRAS, 329, 897
Ibata R., Sollima A., Nipoti C., Bellazzini M., Chapman S. C., Dalessandro E., 2011a, ApJ, 738, 186
Ibata R., Sollima A., Nipoti C., Bellazzini M., Chapman S. C., Dalessandro E., 2011b, ApJ, 743, 43
Ibata R., Nipoti C., Sollima A., Bellazzini M., Chapman S. C., Dalessandro E., 2013, MNRAS, 428, 3648
Ibata R., Thomas G., Famaey B., Malhan K., Martin N., Monari G., 2020, ApJ, 891, 161
Jeřábková T., Hasani Zonoozi A., Kroupa P., Beccari G., Yan Z., Vazdekis A., Zhang Z. Y., 2018, A&A, 620, A39

Jerabkova T., Boffin H. M. J., Beccari G., Anderson R. I., 2019, MNRAS, 489, 4418
Jerabkova T., Boffin H. M. J., Beccari G., de Marchi G., de Bruijne J. H. J., Prusti T., 2021, A&A, 647, A137
Joncour I., Duchêne G., Moraux E., Motte F., 2018, A&A, 620, A27
Just A., Berczik P., Petrov M. I., Ernst A., 2009, MNRAS, 392, 969
Keim M. A. et al., 2022, ApJ, 935, 160
Kokubo E., Yoshinaga K., Makino J., 1998, MNRAS, 297, 1067
Kraus A. L., Hillenbrand L. A., 2007, AJ, 134, 2340
Krause M. G. H., Charbonnel C., Bastian N., Diehl R., 2016, A&A, 587, A53
Kroupa P., 1995a, MNRAS, 277, 1491
Kroupa P., 1995b, MNRAS, 277, 1507
Kroupa P., 1995c, MNRAS, 277, 1522
Kroupa P., 1997, New A, 2, 139
Kroupa P., 1998, MNRAS, 300, 200
Kroupa P., 2001, MNRAS, 322, 231
Kroupa P., 2008, The Cambridge N-Body Lectures, Lecture Notes in Physics, Vol. 760. Springer-Verlag, Berlin Heidelberg, p. 181
Kroupa P., 2015, Can. J. Phys., 93, 169
Kroupa P., Boily C. M., 2002, MNRAS, 336, 1188
Kroupa P., Bouvier J., 2003, MNRAS, 346, 343
Kroupa P., Aarseth S., Hurley J., 2001, MNRAS, 321, 699
Kroupa P., Weidner C., Pflamm-Altenburg J., Thies I., Dabringhausen J., Marks M., Maschberger T., 2013, Planets, Stars and Stellar Systems, Vol. 5. Springer Science+Business Media, Dordrecht, p. 115
Kroupa P. et al., 2018, Nature, 561, E4
Kuhn M. A., Hillenbrand L. A., Carpenter J. M., Avelar Menendez A. R., 2020, ApJ, 899, 128
Küpper A. H. W., MacLeod A., Heggie D. C., 2008, MNRAS, 387, 1248
Küpper A. H. W., Kroupa P., Baumgardt H., Heggie D. C., 2010, MNRAS, 401, 105
Küpper A. H. W., Lane R. R., Heggie D. C., 2012, MNRAS, 420, 2700
Küpper A. H. W., Balbinot E., Bonaca A., Johnston K. V., Hogg D. W., Kroupa P., Santiago B. X., 2015, ApJ, 803, 80
Lada C. J., Lada E. A., 2003, ARA&A, 41, 57
Lelli F., McGaugh S. S., Schombert J. M., 2016, ApJ, 816, L14
Lelli F., McGaugh S. S., Schombert J. M., Pawlowski M. S., 2017, ApJ, 836, 152
Loeb A., 2022a, RNAAS, 6, 55
Loeb A., 2022b, RNAAS, 6, 101
Londrillo P., Nipoti C., 2009, Mem. S.A. it. Suppl., 13, 89
Lüghausen F., Famaey B., Kroupa P., Angus G., Combes F., Gentile G., Tiret O., Zhao H., 2013, MNRAS, 432, 2846
Lüghausen F., Famaey B., Kroupa P., 2014, MNRAS, 441, 2497
Lüghausen F., Famaey B., Kroupa P., 2015, Can. J. Phys., 93, 232
Mahani H., Zonoozi A. H., Haghi H., Jeřábková T., Kroupa P., Mieske S., 2021, MNRAS, 502, 5185
Mapelli M., 2017, MNRAS, 467, 3255
Marks M., Kroupa P., 2011, MNRAS, 417, 1702
Marks M., Kroupa P., 2012, A&A, 543, A8
Marks M., Kroupa P., Baumgardt H., 2008, MNRAS, 386, 2047
Marks M., Kroupa P., Dabringhausen J., Pawlowski M. S., 2012, MNRAS, 422, 2246
McGaugh S. S., 2005, ApJ, 632, 859
McGaugh S., Milgrom M., 2013, ApJ, 766, 22
McGaugh S. S., Schombert J. M., Bothun G. D., de Blok W. J. G., 2000, ApJ, 533, L99
McGaugh S. S., Lelli F., Schombert J. M., 2016, Phys. Rev. Lett., 117, 201101
Megeath S. T. et al., 2016, AJ, 151, 5
Meingast S., Alves J., 2019, A&A, 621, L3
Meingast S., Alves J., Rottensteiner A., 2021, A&A, 645, A84
Merritt D., 2020, A Philosophical Approach to MOND: Assessing the Milgromian Research Program in Cosmology. Cambridge Univ. Press, Cambridge
Mikkola S., Aarseth S. J., 1990, Celest. Mech. Dyn. Astron., 47, 375
Mikkola S., Aarseth S. J., 1993, Celest. Mech. Dyn. Astron., 57, 439
Mikkola S., Aarseth S. J., 1996, Celest. Mech. Dyn. Astron., 64, 197
Milgrom M., 1983, ApJ, 270, 365
Milgrom M., 1999, Phys. Lett. A, 253, 273
Milgrom M., 2010, MNRAS, 403, 886
Milgrom M., 2014, Scholarpedia, 9, 31410
Milgrom M., 2022, Phys. Rev. D, 106, 064060
Misgeld I., Hilker M., 2011, MNRAS, 414, 3699
Miville-Deschênes M.-A., Murray N., Lee E. J., 2017, ApJ, 834, 57
Moeckel N., Bate M. R., 2010, MNRAS, 404, 721
Montes M., Trujillo I., Infante-Sainz R., Monelli M., Borlaff A. S., 2021, ApJ, 919, 56
Nagesh S. T., Banik I., Thies I., Kroupa P., Famaey B., Wittenburg N., Parziale R., Haslbauer M., 2021, Can. J. Phys., 99, 607
Odenkirchen M. et al., 2001, ApJ, 548, L165
Odenkirchen M. et al., 2003, AJ, 126, 2385
Oh S., Evans N. W., 2020, MNRAS, 498, 1920
Oria P. A. et al., 2021, ApJ, 923, 68
Pflamm-Altenburg J., Kroupa P., 2008, Nature, 455, 641
Pflamm-Altenburg J., González-Lópezlira R. A., Kroupa P., 2013, MNRAS, 435, 2604
Pittordis C., Sutherland W., 2022, preprint (arXiv:2205.02846)
Plummer H. C., 1911, MNRAS, 71, 460
Porras A., Christopher M., Allen L., Di Francesco J., Megeath S. T., Myers P. C., 2003, AJ, 126, 1916
Portegies Zwart S., McMillan S. L. W., van Elteren E., Pelupessy I., de Vries N., 2013, Comput. Phys. Commun., 184, 456
Read J. I., Wilkinson M. I., Evans N. W., Gilmore G., Kleyna J. T., 2006, MNRAS, 366, 429
Reinoso B., Fellhauer M., Véjar R., 2018, MNRAS, 476, 1869
Röser S., Schilbach E., 2019, A&A, 627, A4
Röser S., Schilbach E., Piskunov A. E., Kharchenko N. V., Scholz R. D., 2011, A&A, 531, A92
Röser S., Schilbach E., Goldman B., 2019, A&A, 621, L2
Roshan M., Ghafourian N., Kashfi T., Banik I., Haslbauer M., Cuomo V., Famaey B., Kroupa P., 2021, MNRAS, 508, 926
Sanders R., 2007, The Invisible Universe: Dark Matter and Dark Energy. Lecture Notes in Physics, Vol. 720. Springer, Berlin, Heidelberg, p. 375
Sanders R. H., 2012, MNRAS, 422, L21
Sanders R. H., 2015, Can. J. Phys., 93, 126
Sanders R. H., McGaugh S. S., 2002, ARA&A, 40, 263
Scarpa R., 2006, in Lerner E. J., Almeida J. B., eds, AIP Conf. Proc. Vol. 822, First Crisis in Cosmology Conference. Am. Inst. Phys., New York, p. 253
Scarpa R., Marconi G., Carraro G., Falomo R., Villanova S., 2011, A&A, 525, A148
Scarpa R., Ottolina R., Falomo R., Treves A., 2017, Int. J. Mod. Phys. D, 26, 1750067
Sollima A., 2020, MNRAS, 495, 2222
Sollima A., Nipoti C., Mastrobuono Battisti A., Montuori M., Capuzzo-Dolcetta R., 2012a, ApJ, 744, 196
Sollima A., Bellazzini M., Lee J. W., 2012b, ApJ, 755, 156
Stadtler T., Kroupa P., Schmid M., 2021, Can. J. Phys., 99, 222
Strömberg G., 1939, Popular Astronomy, 47, 172
Tang S.-Y. et al., 2019, ApJ, 877, 12
Teyssier R., 2002, A&A, 385, 337
Thomas G. F., Famaey B., Ibata R., Renaud F., Martin N. F., Kroupa P., 2018, A&A, 609, A44
Tiongco M. A., Vesperini E., Varri A. L., 2016, MNRAS, 461, 402
Tiongco M. A., Vesperini E., Varri A. L., 2017, MNRAS, 469, 683
Tiongco M. A., Vesperini E., Varri A. L., 2018, MNRAS, 475, L86
Tiongco M., Collier A., Varri A. L., 2021, MNRAS, 506, 4488
Tiongco M. A., Vesperini E., Varri A. L., 2022, MNRAS, 512, 1584
Trippe S., 2014, Zeitschrift Naturforschung Teil A, 69, 173
van Leeuwen F., 2009, A&A, 497, 209
Verlinde E., 2011, J. High Energy Phys., 2011, 29
von Hoerner S., 1963, ZAp, 57, 47
Wang L., Jerabkova T., 2021, A&A, 655, A71

Wang L., Kroupa P., Jerabkova T., 2019, MNRAS, 484, 1843
Wang L., Iwasawa M., Nitadori K., Makino J., 2020, MNRAS, 497, 536
Wang L., Tanikawa A., Fujii M. S., 2022, MNRAS, 509, 4713
Wirth H., Kroupa P., Haas J., Jerabkova T., Yan Z., Šubr L., 2022, MNRAS, 516, 3342
Wright N. J. et al., 2019, MNRAS, 486, 2477
Wu X., Kroupa P., 2013, MNRAS, 435, 728
Wu X., Kroupa P., 2018, ApJ, 853, 60
Wu X., Kroupa P., 2019, MNRAS, 487, 4012
Wu X., Famaey B., Gentile G., Perets H., Zhao H., 2008, MNRAS, 386, 2199
Wu X., Zhao H., Famaey B., 2010, J. Cosmology Astropart. Phys., 2010, 010
Wu X., Wang Y., Feix M., Zhao H., 2017, ApJ, 844, 130
Yan Z., Jeřábková T., Kroupa P., 2021, A&A, 655, A19
Zonoozi A. H., Lieberz P., Banik I., Haghi H., Kroupa P., 2021, MNRAS, 506, 5468
Zucker C. et al., 2022, Nature, 601, 334

APPENDIX A: ESTIMATION OF THE ORBITAL ECCENTRICITY FROM ONE SNAPSHOT

The periods of the oscillation of the Galactocentric distance of the open star clusters of interest are of the order of 100 Myr. Within the current age of the open star clusters ($\lesssim$800 Myr) only a few apo- and perigalacticon passages occur, and thus only a few orbital eccentricities can be calculated directly from equation (2). In order to better track the evolution of the radial eccentricity in the simulations, it is desirable to estimate the eccentricity at each time-step, given only the actual position $\vec{R} = (\mathrm{X}, \mathrm{Y}, \mathrm{Z})$ and velocity vector $\vec{V} = (V_\mathrm{X}, V_\mathrm{Y}, V_\mathrm{Z})$ of the star cluster centre in the Galactic rest frame.

The eccentricity at a certain snapshot of the orbit is defined by

$$e_{\rm snap} = \frac{R_{\rm aposn} - R_{\rm perisn}}{R_{\rm aposn} + R_{\rm perisn}}, \tag{A1}$$

where $R_{\rm perisn}$ is the perigalactic and $R_{\rm aposn}$ the apo-galactic distance estimated in the following from the snapshot. By having flat rotation curves, galaxies are observationally inferred to be sourcing a logarithmic potential. The Hamiltonian in polar coordinates of a particle with mass m moving in the X-Y-plane of a logarithmic potential with circular velocity, $v_{\rm circ}$, is

$$H = \frac{P_R^2}{2\,m} + \frac{P_\varphi^2}{2\,m\,R^2} + m\,v_{\rm circ}^2 \ln(R), \tag{A2}$$

where R is the radial distance to the Galactic centre, P_R the radial momentum, and P_φ the azimuthal momentum. As H is time independent H is conserved. After mass-normalization we get

$$\frac{H}{m} = \frac{(P_R/m)^2}{2} + \frac{(P_\varphi/m)^2}{2R^2} + v_{\rm circ}^2 \ln(R) = \text{const.} \tag{A3}$$

Because P_φ is cyclic the Z-component of the angular momentum, L_z, is conserved,

$$P_\varphi/m = L_\mathrm{Z}/m = X\,V_\mathrm{Y} - Y\,V_\mathrm{X} = \text{const.} \tag{A4}$$

Expressing the radial momentum by

$$P_\mathrm{R}/m = \dot{R} = \frac{\vec{R} \bullet \vec{V}}{R}, \tag{A5}$$

we obtain for the two turning points R_t with $\dot{R}_\mathrm{t} = 0$

$$\frac{\dot{R}^2}{2} + \frac{(L_\mathrm{Z}/m)^2}{2\,R^2} + v_{\rm circ}^2 \ln(R) = \text{const.} = \frac{(L_\mathrm{Z}/m)^2}{2\,R_\mathrm{t}^2} + v_{\rm circ}^2 \ln(R_\mathrm{t}). \tag{A6}$$

The solution of this trancendental equation requires a numerical method. As there are two turning points (except for the case of a cirular orbit), a numerical root finding algorithm requires appropriate starting points for the iteration. These points can be obtained by fitting this equation locally up to second order, and can be also used as approximations of the turning points.

The Galactocentric distance, R_t, of each turning point is expressed as the sum of the current Galactocentric distance, R, and the radial distance, δR, from the current position to the Galactocentric distance of the respective turning point, $R_\mathrm{t} = R + \delta R$ along the line Galactic centre to cluster, where δR is positive in case of the apo-galactic turning point and negative in case of the peri-galactic turning point. After normalization of the radial distance, $x = \delta R/R$, i.e.

$$R_\mathrm{t} = R(1 + x), \tag{A7}$$

we get

$$\frac{\dot{R}^2}{2} + \frac{(L_\mathrm{Z}/m)^2}{2\,R^2} = \frac{(L_\mathrm{Z}/m)^2}{2\,R^2}(1 + x)^{-2} + v_{\rm circ}^2 \ln(1 + x). \tag{A8}$$

This yields a solution for x, a positive one for the peri-galactic and a negative for the apo-galactic turning point.

Given that $|\delta R| \ll R$, the full solution (equation A8) can be simplified: For a star cluster of current interest the Galacticentric distance is $R \approx 8.3$ kpc and $|\delta R|$ is of the order of $\lesssim$ few hundred pc. Thus, as $|x| \ll 1$, both x-terms can be Taylor expanded,

$$(1 + x)^{-2} = 1 - 2x + 3x^2 - \ldots, \quad \text{for } |x| < 1, \tag{A9}$$

and

$$\ln(1 + x) = x - \frac{1}{2}x^2 + \ldots, \quad \text{for } |x| < 1, \tag{A10}$$

and are truncated after the second order. Introducing the abbreviations

$$\eta = \frac{\dot{R}^2}{2} \quad \text{and} \quad \mu = \frac{(L_\mathrm{Z}/m)^2}{2\,R^2}, \tag{A11}$$

a quadratic equation for x emerges,

$$\eta + \mu = \mu(1 - 2x + 3x^2) + v_{\rm circ}^2 \left(x - \frac{1}{2}x^2\right), \tag{A12}$$

with two solutions

$$x_{1/2} = \frac{-b \pm \sqrt{b^2 - 4\,a\eta}}{2\,a}, \tag{A13}$$

and parameters

$$a = \frac{v_{\rm circ}^2}{2} - 3\mu \quad \text{and} \quad b = 2\mu - v_{\rm circ}^2. \tag{A14}$$

Using equation (A7) the first solution for x having the plus sign in front of the square root determines the Galactocentric distance of the apo-galactic turning point, the second solution for x the Galactocentric distance of the peri-galactic turning point.

We test the accuracy of the approximating method for a logarithmic potential with a rotational velocity of $v_{\rm circ} = 250\,\mathrm{km\,s^{-1}}$ (this is for consistency with the models of Sections 4 and 5, while the data in Table 1 assume $v_{\rm circ} = 220\,\mathrm{km\,s^{-1}}$) and local radial velocity of $10\,\mathrm{km\,s^{-1}}$ at a galactocentric distance of 8.5 kpc, which are typical data of solar neighbourhood star clusters. Assume the actual position and velocity vectors in the Galactic rest frame are $\vec{R} = (8500, 0, 0)$ pc and $\vec{V} = (10.23, 255.65, 0)\,\mathrm{pc\,Myr^{-1}}$. The complete solution of equation (A8) leads to peri- and apocentre distances of $R_{\rm aposn} = 8740.4$ pc and $R_{\rm perisn} = 8259.6$ pc and an orbital eccentricity $e_{\rm snap} = 0.0282823$.

With the approximative solution (equations A4, A11, A14, A13, and A7, in this order), we obtain $R_{\rm aposn} = 8746.2\,{\rm pc}$ and $R_{\rm perisn} = 8265.1\,{\rm pc}$ giving an orbital eccentricity of $e_{\rm snap} = 0.0282812$. In this case, the relative error of the eccentricity is 4×10^{-5}.

These approximative solutions of the two turning points

$$R_{\rm t_1} = R(1 + x_1), \quad R_{\rm t_2} = R(1 + x_2) \tag{A15}$$

can be used as starting points $R_1 = R_{\rm t_1}$ and $R_1 = R_{\rm t_2}$ for the Newton–Raphson root finding algorithm with iterative step

$$R_{n+1} = R_n - \frac{f(R_n)}{f'(R_n)}, \tag{A16}$$

where the function, of which the roots are to be found, is

$$f(R_n) = \frac{\dot{R}^2}{2} + \frac{(L_{\rm Z}/m)^2}{2\,R^2} + V_{\rm circ}^2 \ln(R) - \frac{(L_{\rm Z}/m)^2}{2\,R_n^2} - V_{\rm circ}^2 \ln(R_n) \tag{A17}$$

and its primitive

$$f'(R_n) = \frac{(L_{\rm Z}/m)^2}{R_n^3} - \frac{V_{\rm circ}}{R_n}. \tag{A18}$$

It turns out, that two or three steps are sufficient.

This paper has been typeset from a TEX/LATEX file prepared by the author.